SANDIA REPORT

SAND2003-8804
Unlimited Release
Printed January 2004

A mechanism-based approach to modeling ductile fracture

P.A. Klein, S.X. McFadden, D.J. Bammann, Y. Hammi, J.W. Foulk, B.R. Antoun

Prepared by
Sandia National Laboratories
Albuquerque, New Mexico 87185 and Livermore, California 94550

Sandia is a multiprogram laboratory operated by Sandia Corporation,
a Lockheed Martin Company, for the United States Department of Energy's
National Nuclear Security Administration under Contract DE-AC04-94AL85000.

Sandia National Laboratories

Issued by Sandia National Laboratories, operated for the United States Department of Energy by Sandia Corporation.

Available to DOE and DOE contractors from
U.S. Department of Energy
Office of Scientific and Technical Information
P.O. Box 62
Oak Ridge, TN 37831

Telephone: (865)576-8401
Facsimile: (865)576-5728
E-Mail: reports@adonis.osti.gov
Online ordering: http://www.doe.gov/bridge

Available to the public from
U.S. Department of Commerce
National Technical Information Service
5285 Port Royal Rd
Springfield, VA 22161

Telephone: (800)553-6847
Facsimile: (703)605-6900
E-Mail: orders@ntis.fedworld.gov
Online order: http://www.ntis.gov/help/ordermethods.asp?loc=7-4-0#online

SAND2003-8804
Unlimited Release
Printed January 2004

A mechanism-based approach to modeling ductile fracture

P.A. Klein, S.X. McFadden, D.J. Bammann, Y. Hammi, J.W. Foulk, B.R. Antoun

Sandia National Laboratories
P.O. Box 969
Livermore, CA 94551

Abstract

Ductile fracture in metals has been observed to result from the nucleation, growth, and coalescence of voids. The evolution of this damage is inherently history dependent, affected by how time-varying stresses drive the formation of defect structures in the material. At some critically damaged state, the softening response of the material leads to strain localization across a surface that, under continued loading, becomes the faces of a crack in the material. Modeling localization of strain requires introduction of a length scale to make the energy dissipated in the localized zone well-defined. In this work, a cohesive zone approach is used to describe the post-bifurcation evolution of material within the localized zone. The relations are developed within a thermodynamically consistent framework that incorporates temperature and rate-dependent evolution relationships motivated by dislocation mechanics. As such, we do not prescribe the evolution of tractions with opening displacements across the localized zone *a priori*. The evolution of tractions is itself an outcome of the solution of particular, initial boundary value problems. The stress and internal state of the material at the point of bifurcation provides the initial conditions for the subsequent evolution of the cohesive zone. The models we develop are motivated by *in-situ* scanning electron microscopy of three-point bending experiments using 6061-T6 aluminum and 304L stainless steel. The *in situ* observations of the initiation and evolution of fracture zones reveal the scale over which the failure mechanisms act. In addition, these observations are essential for motivating the micromechanically-based models of the decohesion process that incorporate the effects of loading mode mixity, temperature, and loading rate. The response of these new cohesive zone relations is demonstrated by modeling the three-point bending configuration used for the experiments. In addition, we survey other methods with the potential to provide more detailed information about the near tip deformation fields.

Keywords: cohesive modeling, ductile fracture, state variable plasticity, continuum damage mechanics.

This page intentionally left blank.

Contents

List of Figures

Chapter 1

Introduction

Cohesive approaches to modeling fracture are attractive because they allow material-specific deformation mechanisms to be developed into models of failure. This attribute is especially useful for application to modeling fracture in ductile materials because the dissipation associated with crack growth cannot be reduced to a failure criterion. The origins of cohesive methods can be traced to the work of Prandtl [17] in which a cohesive traction relation is employed to predict the length of the debonded zone between two slender beams. Xu and Needleman [31] pioneered the incorporation of cohesive methods in finite element simulations by including the effect of a network of cohesive surfaces within the statement of virtual work. They also present a mixed-mode traction-separation relationship that has been widely used in the study of brittle fracture. This cohesive relation does not represent any specific mechanisms of material failure, but instead defines a generic dissipation associated with the creation of new surfaces. By incorporating the essential features of finite material strength and finite work to fracture, the relation produces fracture in simulations without enforcing a presumed fracture criteria.

Fracture in ductile metals has long been associated with the nucleation, growth, and coalescence of voids that evolve through plastic deformation. A number of approaches have been used to apply cohesive methods to the study of ductile fracture, though none have incorporated this complete multi-stage view driven by void evolution. The simplest approach is to combine a generic cohesive model to represent the fracture behavior with a ductile constitutive model for the bulk response. In studies like [24, 19, 5], the generic models are adaptive of application to ductile fracture by making the same parameters used to characterize brittle fracture, cohesive strength and characteristic opening displacement, dependent on rate, history, and stress-state dependent parameters. The parameters are selected so that the combined dissipation in the cohesive zone and surrounding bulk material matches the experimentally determined work to fracture for the material. Some characteristics of void growth have been introduced in cohesive parameters [27, 18] by relating them to the Gurson model [8]. Even in these cases, the shape of the traction evolution has an explicit, predetermined functional form that does not possess any rate, history, or mode mixity effects specific to the failure mechanisms in ductile metals.

To address these shortcomings, we have developed mechanism-based cohesive relations for modeling ductile fracture which are complementary to an internal state variable plasticity model

for metals [2]. The details of the bulk plasticity model will not be covered here. However, some aspects of the formulation are discussed in order to show how specific effects have been incorporated in the cohesive relations. In the bulk constitutive model, hardening with the evolution of plastic deformation is captured by a state variable representing the density of statistically stored dislocations. Under monotonic loading, the density of statistically stored dislocations increases, acting to increase the flow stress in the material. Through the addition of evolution equations describing hardening and recovery, the model has been successful in predicting material behavior for multi-stage tests over a range of temperature and strain rates. Degradation in the material due to the evolution of voids is characterized by a damage parameter which represents the void volume fraction within the context of continuum damage mechanics [14].

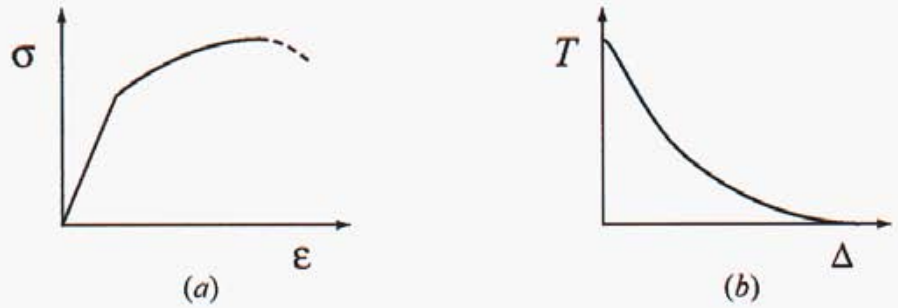

Figure 1.1: The complementary relationship between a bulk constitutive model that exhibits softening and a cohesive relation to describe the post-bifurcation response.

As depicted in Figure 1.1, the cohesive relations serve as a complement to the bulk constitutive model at the onset of softening. Macroscopic softening is associated with the coalescence of voids at incipient internal necking of the intervening matrix [22]. The point of bifurcation shown in Figure 1.1(a) can be determined rigorously from a stability analysis [10]; however, we identify this state approximately by assuming a critically damaged void volume fraction. In the post bifurcation regime, deformation becomes localized across a surface, or void sheet, which we describe with a cohesive relation as shown in Figure 1.1(b), until complete failure occurs. The *in situ* scanning eletron microscope (SEM) micrographs in Figure 1.2 show the linkage of voids ahead of a growing crack in 6061-T6 aluminum. The width of the localized zone of deformation emerges as a length scale controlling the amount of dissipation. The cohesive relations furnish this length scale, making the dissipation associated with the localized deformation well-defined. The cohesive relations are formulated as mixed-mode evolution equations for the opening and shear displacements of the zone. The material state at the point of localization provides the initial conditions for the evolution of the fracture process zone. The evolution of the tractions is not defined *a priori*, but is determined in response to the loads applied to the zone.

The cohesive relations are presented in the following sequence. First, the thermodynamic description of the cohesive zone relations is outlined to define the kinematics of deformation, the internal state variables, and their work conjugates. Subsequently, we present a general algorithm by which traction are integrated, and apply the algorithm to a pair of mechanism-based evolution

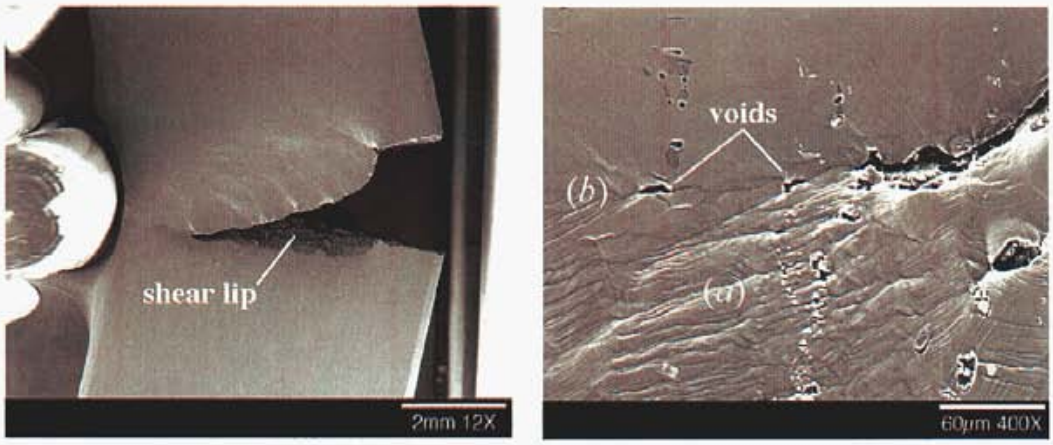

Figure 1.2: *In situ* micrographs showing the void mechanisms associated with fracture in ductile metals.

equations, demonstrating their characteristics with simple calculations. Next, we describe the experiments that were conducted in order to motivate the evolution relations used for the cohesive models, as well as to provide macroscopic experimental measurements for validating the models. We also describe some experimental methods that may prove useful in the future for providing the detailed information about near tip deformation field needed to improve the cohesive models. Finally, we present a series of calculations to demonstrate the capabilities of the modeling approach, including simulations of the three-point bending geometry used in the experiments.

This page intentionally left blank.

Chapter 2

Cohesive zone model formulation

We begin by presenting cohesive zone formulations within the variational setting that is the basis for finite element methods. Over a region described in its undeformed configuration as having a domain Ω, a boundary Γ, and a density ρ, the variational form of the linear momentum balance, in the absence of body forces, is

$$\int_{\Omega} \rho \frac{\partial^2 \mathbf{u}}{\partial t^2} \cdot \delta \mathbf{u} \, d\Omega + \int_{\Omega} \mathbf{P}{:}\delta \mathbf{F} \, d\Omega + \int_{\Gamma_{\text{int}}} \mathbf{T} \cdot \delta \boldsymbol{\Delta} \, d\Gamma = \int_{\Gamma_h} \mathbf{T} \cdot \delta \mathbf{u} \, d\Gamma, \tag{2.1}$$

where $\delta \mathbf{u}$, $\delta \mathbf{F}$, and, $\delta \boldsymbol{\Delta}$ are the variations in the displacement, deformation gradient, and relative opening displacement, respectively, $\mathbf{P}$ is the nonsymmetric 1st Piola-Kirchhoff stress, and $\mathbf{T} = \mathbf{PN}$ is the force per unit undeformed area with normal $\mathbf{N}$. Kinematic boundary conditions are satisfied in the selection of functions used to represent $\mathbf{u}$, and traction boundary conditions produce the contribution to (2.1) over Γ_h. Tractions acting across internal surfaces produce the contribution over Γ_{int}. Solutions to (2.1) are then uniquely determined by specification of initial and boundary conditions. The discussion that follows describes the origin of the $\mathbf{T}$-$\boldsymbol{\Delta}$ conjugate pair.

2.1 Thermodynamic considerations

We begin the thermodynamic development with a statement of the first law

$$\int_{\Omega} \rho \frac{\partial W}{\partial t} \, d\Omega = \int_{\Omega} \mathbf{P}{:}\dot{\mathbf{F}} \, d\Omega - \int_{\Gamma} \mathbf{Q} \cdot \mathbf{N} \, d\Gamma + \int_{\Omega} \rho R \, d\Omega, \tag{2.2}$$

where ρ is the mass density, W is the internal energy per unit mass, $\mathbf{P}$ is the 1st Piola-Kirchhoff stress, $\mathbf{F}$ is the deformation gradient, $\mathbf{Q}$ is the heat flux into Ω, $\mathbf{N}$ is the outward normal to Γ, and R is the internal heat supply per unit mass. Then, we restrict the body Ω to a strip of width w with surfaces Γ. With this assumption, the first law becomes

$$w \int_{\Gamma} \rho \frac{\partial W}{\partial t} \, d\Gamma = w \int_{\Gamma} \mathbf{P}{:}\dot{\mathbf{F}} \, d\Gamma - \int_{\Gamma} [\![\mathbf{Q} \cdot \mathbf{N}]\!] \, d\Gamma + w \int_{\Gamma} \rho R \, d\Gamma, \tag{2.3}$$

Neglecting rotations, $\dot{\mathbf{F}}$ across the strip reduces to

$$\dot{\mathbf{F}} = w\dot{\lambda}\mathbf{n} \otimes \mathbf{N}, \tag{2.4}$$

where $\dot{\lambda}$ is the stretch rate normal to the surface. Using this result, the stress work term may be rewritten as

$$w\mathbf{P}:\dot{\mathbf{F}} = (\mathbf{PN}) \cdot \left(w\dot{\lambda}\mathbf{n}\right). \tag{2.5}$$

Noting that $\mathbf{T} = \mathbf{PN}$ and $\dot{\boldsymbol{\Delta}} = \left(w\dot{\lambda}\mathbf{n}\right)$, the stress work expression reduces to

$$w\mathbf{P}:\dot{\mathbf{F}} = \mathbf{T} \cdot \dot{\boldsymbol{\Delta}}, \tag{2.6}$$

where $\boldsymbol{\Delta}$ is the displacement jump across the strip. With this result, we can localize the energy balance pointwise as

$$[\![\mathbf{Q} \cdot \mathbf{N}]\!] = w\mathbf{T} \cdot \dot{\boldsymbol{\Delta}} + w\rho\left(R - \frac{\partial W}{\partial t}\right). \tag{2.7}$$

The second law of thermodynamics states that over a body Ω the rate of entropy increase must be equal to or greater than the entropy input rate, as expressed by

$$\frac{d}{dt}\int_{\Omega} \eta\rho \, d\Omega \geq \int_{\Omega} \frac{R}{\theta}\rho \, d\Omega - \int_{\Gamma} \frac{\mathbf{Q}}{\theta} \cdot \mathbf{N} \, d\Omega, \tag{2.8}$$

where η is the entropy per unit mass and θ is the absolute temperature. Again, restricting the body to a strip of width w, we find

$$w\int_{\Gamma} \rho\frac{\partial \eta}{\partial t} \, d\Gamma \geq w\int_{\Gamma} \frac{r}{\theta}\rho \, d\Gamma - \int_{\Gamma} \frac{1}{\theta}[\![\mathbf{Q} \cdot \mathbf{N}]\!] \, d\Gamma, \tag{2.9}$$

which yields

$$w\rho\frac{\partial \eta}{\partial t} \geq \frac{G}{\theta}w\rho - \frac{1}{\theta}[\![\mathbf{Q} \cdot \mathbf{N}]\!]. \tag{2.10}$$

following localization of the integral.

The thermodynamic description we employ for the cohesive zone follows the internal state variable theory of Coleman and Gurtin [4]. In accordance with the description of the surrounding bulk material [2], we assume the Helmholtz free energy Ψ for the material is a function of the elastic part of the opening displacement $\boldsymbol{\Delta}^e$, internal state variables $\mathbf{q}$, the void volume fraction ϕ, and the absolute temperature θ. Hence, we assume

$$\Psi = \Psi\left(\boldsymbol{\Delta}^e, \mathbf{q}, \phi, \theta\right), \tag{2.11}$$

where the deformation of the zone is given by the opening displacement

$$\boldsymbol{\Delta} = \boldsymbol{\Delta}^e + \boldsymbol{\Delta}^p, \tag{2.12}$$

which is additively decomposed into an elastic, or reversible, part $\boldsymbol{\Delta}^e$ and an inelastic part $\boldsymbol{\Delta}^p$. The Helmholtz free energy Ψ is defined as

$$\Psi = W - \eta\theta. \tag{2.13}$$

Expanding $\dot{\Psi}$ from (2.13), we have

$$\frac{\partial \Psi}{\partial \boldsymbol{\Delta}^e} \cdot \dot{\boldsymbol{\Delta}}^e + \frac{\partial \Psi}{\partial \mathbf{q}} \cdot \dot{\mathbf{q}} + \frac{\partial \Psi}{\partial \phi} \cdot \dot{\phi} + \frac{\partial \Psi}{\partial \theta}\dot{\theta} = \frac{\partial W}{\partial t} - \frac{\partial \eta}{\partial t}\theta - \eta\dot{\theta}. \tag{2.14}$$

Substituting this result into (2.10) and using $\frac{\partial W}{\partial t}$ from (2.7) yields

$$\mathbf{T} \cdot \left(\dot{\boldsymbol{\Delta}}^p + \dot{\boldsymbol{\Delta}}^e\right) - \frac{\partial \Psi}{\partial \boldsymbol{\Delta}^e} \cdot \dot{\boldsymbol{\Delta}}^e - \frac{\partial \Psi}{\partial \mathbf{q}}\dot{\mathbf{q}} - \frac{\partial \Psi}{\partial \phi}\dot{\phi} - \left(\frac{\partial \Psi}{\partial \theta} + \eta\right)\dot{\theta} \geq 0, \tag{2.15}$$

from which we conclude

$$T = \frac{\partial \Psi}{\partial \boldsymbol{\Delta}^e}, \tag{2.16}$$

$$\eta = -\frac{\partial \Psi}{\partial \theta}, \tag{2.17}$$

which define the traction $\mathbf{T}$ and entropy η, respectively. The remaining terms yield the reduced dissipation inequality

$$\mathbf{T} \cdot \dot{\boldsymbol{\Delta}}^p - \frac{\partial \Psi}{\partial \mathbf{q}}\dot{\mathbf{q}} - \frac{\partial \Psi}{\partial \phi}\dot{\phi} \geq 0. \tag{2.18}$$

As with the description of the surrounding bulk, evolution equations must now be defined for the kinematic variables $\boldsymbol{\Delta}^p$, $\mathbf{q}$, and ϕ. In particular, we will assume rigid-inelastic response for the zone, meaning we assume negligible elastic opening displacement $\boldsymbol{\Delta}^e$. We make this assumption based on *in-situ* SEM observations of fracture process zones in 6061 aluminum and 304L stainless steel. By making this assumption, we avoid the issue of defining how strain energy is stored by the highly deformed material in the zone which is needed to evaluate $\mathbf{T} = \frac{\partial \Psi}{\partial \boldsymbol{\Delta}^e}$. In the sections that follow, we will show that is it not necessary to define the traction acting on the zone through (2.16). The traction in the zone can be determined through solving the discrete evolution equations, driven by the deformation imposed by the surrounding bulk. In effect, the traction in the zone is determined by bringing the zone into equilibrium with the stresses in the surrounding material.

2.2 Traction integration

The mixed-mode evolution of the cohesive zone is determined by a series of rate equations

$$\dot{\boldsymbol{\Delta}} = \dot{\boldsymbol{\Delta}}(\mathbf{T}, \mathbf{q}, \boldsymbol{\Delta}), \tag{2.19}$$

$$\dot{\mathbf{q}} = \dot{\mathbf{q}}(\mathbf{T}, \mathbf{q}), \tag{2.20}$$

which describe rate of change in the opening displacement $\boldsymbol{\Delta}$ and the internal state variables $\mathbf{q}$ in terms of the traction $\mathbf{T}$ acting on the zone. With these relations, the traction-separation response $\mathbf{T}(\boldsymbol{\Delta})$ of the zone is not known *a priori* and indeed may vary from point to point along the fracture path as a function of material history in $\mathbf{q}$ prior to the initiation of failure and the load history acting on the fracture process zone subsequent to initiation. For numerical evaluation, the response of the zone is determined through a displacement driven procedure which uses $\{\mathbf{q}_n, \boldsymbol{\Delta}_n\}$ from time t_n to determine $\{\mathbf{T}_{n+1}, \mathbf{q}_{n+1}\}$ at time t_{n+1} driven by the predicted value of $\boldsymbol{\Delta}_{n+1}$. The fully implicit scheme is derived by expressing the rates in terms of the first-order accurate, backward-Euler, finite difference approximations

$$\frac{1}{\Delta t}\left(\boldsymbol{\Delta}_{n+1} - \boldsymbol{\Delta}_n\right) = \dot{\boldsymbol{\Delta}}(\mathbf{T}_{n+1}, \boldsymbol{\Delta}_{n+1}, \mathbf{q}_{n+1}), \tag{2.21}$$

$$\frac{1}{\Delta t}\left(\mathbf{q}_{n+1} - \mathbf{q}_n\right) = \dot{\mathbf{q}}(\mathbf{T}_{n+1}, \mathbf{q}_{n+1}), \tag{2.22}$$

for a time increment Δt. The updated traction and state variables are determined iteratively as

$$\mathbf{T}_{n+1}^{(i+1)} = \mathbf{T}_{n+1}^{(i)} + \delta\mathbf{T}, \tag{2.23}$$

$$\mathbf{q}_{n+1}^{(i+1)} = \mathbf{q}_{n+1}^{(i)} + \delta\mathbf{q}, \tag{2.24}$$

where a local Newton iteration is employed to determine the updates from

$$\begin{Bmatrix} \delta\mathbf{T} \\ \delta\mathbf{q} \end{Bmatrix} = \begin{bmatrix} \frac{\partial \mathbf{R}_T^{(i)}}{\partial \mathbf{T}} & \frac{\partial \mathbf{R}_T^{(i)}}{\partial \mathbf{q}} \\ \frac{\partial \mathbf{R}_q^{(i)}}{\partial \mathbf{T}} & \frac{\partial \mathbf{R}_q^{(i)}}{\partial \mathbf{q}} \end{bmatrix}^{-1} \begin{Bmatrix} \mathbf{R}_T^{(i)} \\ \mathbf{R}_q^{(i)} \end{Bmatrix}, \tag{2.25}$$

where $\mathbf{R}_T^{(i)}$ and $\mathbf{R}_q^{(i)}$ are the residuals of (2.21) and (2.22), respectively,

$$\mathbf{R}_T^{(i)} = \dot{\boldsymbol{\Delta}}\left(\mathbf{T}_{n+1}^{(i)}, \boldsymbol{\Delta}_{n+1}^{(i)}, \mathbf{q}_{n+1}^{(i)}\right) - \frac{1}{\Delta t}\left(\boldsymbol{\Delta}_{n+1}^{(i)} - \boldsymbol{\Delta}_n\right), \tag{2.26}$$

$$\mathbf{R}_q^{(i)} = \dot{\mathbf{q}}\left(\mathbf{T}_{n+1}^{(i)}, \mathbf{q}_{n+1}^{(i)}\right) - \frac{1}{\Delta t}\left(\mathbf{q}_{n+1}^{(i)} - \mathbf{q}_n\right). \tag{2.27}$$

From these expressions, the components of the Jacobian in (2.25) are given by

$$\frac{\partial \mathbf{R}_T}{\partial \mathbf{T}} = \frac{\partial \dot{\boldsymbol{\Delta}}}{\partial \mathbf{T}} \qquad \frac{\partial \mathbf{R}_T}{\partial \mathbf{q}} = \frac{\partial \dot{\boldsymbol{\Delta}}}{\partial \mathbf{q}}, \tag{2.28}$$

$$\frac{\partial \mathbf{R}_q}{\partial \mathbf{T}} = \frac{\partial \dot{\mathbf{q}}}{\partial \mathbf{T}} \qquad \frac{\partial \mathbf{R}_q}{\partial \mathbf{q}} = \frac{\partial \dot{\mathbf{q}}}{\partial \mathbf{q}} - \frac{1}{\Delta t}\mathbf{1}. \tag{2.29}$$

Once the updated state has been found, these values can be used to determined the algorithmic tangent response of the zone by linearizing (2.21) and (2.22) about $\{\mathbf{T}_{n+1}, \boldsymbol{\Delta}_{n+1}, \mathbf{q}_{n+1}\}$. The resulting tangent response is given by

$$\frac{\partial \mathbf{T}_{n+1}}{\partial \boldsymbol{\Delta}_{n+1}} = \left[\frac{\partial \dot{\boldsymbol{\Delta}}}{\partial \mathbf{T}} + \frac{\partial \dot{\boldsymbol{\Delta}}}{\partial \mathbf{q}}\left(\frac{1}{\Delta t}\mathbf{1} - \frac{\partial \dot{\mathbf{q}}}{\partial \mathbf{q}}\right)^{-1}\frac{\partial \dot{\mathbf{q}}}{\partial \mathbf{T}}\right]^{-1}\left(\frac{1}{\Delta t}\mathbf{1} - \frac{\partial \dot{\boldsymbol{\Delta}}}{\partial \boldsymbol{\Delta}}\right), \tag{2.30}$$

where all quantities on the right-hand side are evaluated using the updated values from t_{n+1}.

As a result of the state variable formulation, the traction-separation response of the zone is not defined in an *a priori* form, and the dissipation is path-dependent. At any point along the fracture surface, the path-dependent dissipation required to reach a given state of opening is given by

$$G(\boldsymbol{\Delta}) = \int_0^{\boldsymbol{\Delta}} \mathbf{T}(\boldsymbol{\Delta}') \cdot d\boldsymbol{\Delta}', \tag{2.31}$$

from which we can define the total energy per area dissipated by the zone with crack extension as

$$G_c = \lim_{\|\boldsymbol{\Delta}\| \to \infty} G(\boldsymbol{\Delta}) \tag{2.32}$$

As will be discussed in Section 2.3.3, vanishing tractions ($||\mathbf{T}|| \to 0$ as $||\boldsymbol{\Delta}|| \to \infty$) are not a sufficient condition for guaranteeing that the dissipation will be bounded. With stress driven evolution equations, a competition is established between the rate at which the tractions diminish and the rate at which the failure mechanisms continue to evolve. The condition of boundedness on (2.32) then furnishes limits on the selection of model parameters.

2.3 Mechanism-based cohesive zone relations

Next, we present specific cohesive zone relations that can be combined with the integration scheme of the previous section to perform numerical simulations of ductile crack growth. The relations presented here are motivated by *in situ* SEM observations of crack growth in three-point bending specimens. Although limited to a view of how the cracks progressed on the surface of the specimen, the observations did provide insight into the active deformation mechanisms, the scale of the fracture process zone, and the behavior of the fracture process zone with varying mode-mixity and load reversals. One of the principal assumptions regarding the response of the cohesive zone is that the deformation of the zone is so highly dominated by inelastic mechanisms that the elastic response of the zone can be neglected. Typically, it is the elastic response which is used to determine the traction in the zone. In the absence of elastic deformation, the tractions must be determined iteratively to bring them into equilibrium with the traction acting on the zone due to the surrounding body.

The inelastic response is derived from consideration of the deformation mechanisms and geometric constraints of the zone. An *in situ* SEM micrograph together with its idealized representation is shown in Figure 2.1. We assume that once void growth has reached a critical state, further deformation is localized within a zone, or void sheet. The post-bifurcation behavior is then described using a traction-separation relation rather than a stress-strain description, meaning that a length scale has been introduced to regularize the dissipation of the zone. In this work, we do not attempt to predict the initial width of this zone; instead, this width is parameter of the cohesive zone model, which is estimated based on experimental observations.

The framework for the cohesive relations described in Section 2.2 allows the normal and shear response of the zone to be defined independently to incorporate specific deformation mechanisms.

Figure 2.1: Idealization of the localized fracture process zone. The *in situ* SEM micrograph of 6061 aluminum depicts voids growing ahead of the crack tip. These are represented as a void sheet with initial width w_0.

The expansion of a zone with initial width w_0 in the normal direction is associated with void growth, represented by the void volume fraction

$$\phi = \frac{V_{\text{void}}}{V_{\text{total}}}, \tag{2.33}$$

where the zone is assumed be active for $\phi_{\text{init}} \leq \phi < 1$. The critical void volume fraction ϕ_{init} is the value at which deformation in the material becomes localized within the zone. For $\phi < \phi_{\text{init}}$, the zone is rigid $(\dot{\boldsymbol{\Delta}} = 0)$ and not evolving in any way, and for $\phi = 1$, the material is completely failed and has no load carrying capacity $(\mathbf{T} = 0)$. The total volume of the zone is

$$V_{\text{total}} = \frac{A w_0}{1 - \phi}, \tag{2.34}$$

where A is the in-plane area. Assuming the in-plane area remains constant, we find that the normal opening rate from these geometric arguments is

$$\dot{\Delta}_n = \frac{\dot{\phi}}{(1-\phi)^2} w_0. \tag{2.35}$$

From (2.35), we notice that $\dot{\phi} > 0$ if the normal opening displacement is increasing and $\dot{\phi} < 0$ if the normal opening displacement is decreasing. When subject to compression, the voids in the fracture process zone collapse; however, the surface of the voids may not actually "heal" to produce material in the same state as before deformation due to the attack of environment. If the voids do completely heal, the material loses history from previous loading. To allow the voids in the fracture process zone to expand and collapse reversibly or irreversibly depending on the environmental conditions, we introduce a measure of the irreversible void volume fraction ϕ^*, which evolves as

$$\dot{\phi}^* = \begin{cases} \dot{\phi} & \dot{\phi} > 0, \\ 0 & \dot{\phi} < 0. \end{cases} \tag{2.36}$$

The evolution equations for the void volume fraction $\dot{\phi}$ as well as the shear response of the zone $\dot{\Delta}_t$ are associated with the flow of thermally activated dislocations through classical relations [7, 1]. Particular forms of $\dot{\phi}$ and $\dot{\Delta}_t$ will be presented in Sections 2.3.2 and 2.3.3. These relations will depend on the history-tracking ϕ^*, rather than the geometric factor ϕ. In cases where the damage truly is reversible, one would define

$$\dot{\phi}^* = \dot{\phi}. \tag{2.37}$$

In all cases, the shear response is assumed to be isotropic, that is, the response is defined in terms of the tangential traction and opening

$$T_t = ||\mathbf{T} - (\mathbf{T} \cdot \mathbf{N})\,\mathbf{N}||, \tag{2.38}$$

$$\Delta_t = ||\boldsymbol{\Delta} - (\boldsymbol{\Delta} \cdot \mathbf{N})\,\mathbf{N}||, \tag{2.39}$$

where $\mathbf{N}$ is the process zone normal, independent of orientation within the plane.

The mechanical response of the process zone is coupled to the thermal response in a number of ways beyond the temperature dependence of the parameters incorporated from the associated bulk model, which is discussed in Section 2.3.1. First, the incremental mechanical dissipation in the process zone over a time Δt is related to the heat generation rate as

$$\delta q = \frac{\beta}{\Delta t}\mathbf{T} \cdot \delta\boldsymbol{\Delta}, \tag{2.40}$$

where β is the Taylor-Quinney [21] coefficient, usually given a value of $\beta = 0.9$. The material in the zone itself is assumed to have negligible thermal capacity, so the heat generated in (2.40) is deposited in equal parts onto the bulk on either side of the zone. In the absence of thermal capacity, the flux of heat across the zone is given by

$$q = -k_s(\phi)\,\Delta\theta, \tag{2.41}$$

where k_s is the surface thermal conductivity and $\Delta\theta$ is the jump in the temperature across the zone. Analogous to the load carrying capacity, the thermal conductivity degrades with damage as

$$k_s(\phi) = \frac{k}{w_0}\frac{1-\phi}{1-\phi_{\text{init}}}, \tag{2.42}$$

where k is the thermal conductivity of the undamaged bulk material.

2.3.1 Associated bulk model

For ductile materials, the mechanisms of bulk dissipation and the mechanisms of dissipation within the fracture process zone are intimately connected. For the material model we are considering, which exhibits softening due to degradation, the cohesive zone describes the deformation of the material in the post bifurcation regime. We develop models for the constitutive response of the zone by assuming that the mechanisms of dissipation, namely plasticity, continue to evolve as the material approaches complete failure although the material has weakened to such an extent that homogeneous deformations are no longer stable.

A unified approach to modeling failure in the ductile material should therefore link the dissipation mechanisms of the bulk material with those in the fracture process zone. The bulk model associated with the cohesive relations developed in this work is due to Bammann, Chiesa, and Johnson (BCJ) [1, 2]. Numerous advancements to the model have been made since it was initially proposed. Here, we employ the most basic form of the model, introducing only the aspects which are also incorporated in the cohesive model. The BCJ model is an internal state variable model for metal plasticity that takes into account the hardening effects of statistically stored dislocations that accumulate due to plastic strain, as well as the degrading effects of damage, or porosity, that develops due to stress triaxiality. The rate of plastic deformation for the model is given by

$$\mathbf{d}^p = \sqrt{\frac{3}{2}}\dot{\epsilon}_0(\theta)\sinh\left[\frac{1}{V(\theta)}\left\langle\frac{\sqrt{\frac{3}{2}}\|\boldsymbol{\xi}\|}{1-\phi} - (Y(\theta)+\kappa)\right\rangle\right]\frac{\boldsymbol{\xi}}{\|\boldsymbol{\xi}\|}, \tag{2.43}$$

where θ is the temperature. This expression for the plastic rate of deformation describes the evolution of plasticity due to thermally activated dislocations [2]. The driving force for the evolution of plastic strain is the (deviatoric) relative stress

$$\boldsymbol{\xi} = \mathrm{dev}(\boldsymbol{\sigma}) - \frac{2}{3}\boldsymbol{\alpha}, \tag{2.44}$$

where kinematic hardening arises due to the evolution of the back stress $\boldsymbol{\alpha}$. The effect of the porosity ($0 \leq \phi \leq 1$) is to magnify the driving stress as a result of the associated reduction in load-bearing material. The resistance to plastic flow is expressed in terms of an initial yield stress $Y(\theta)$ and isotropic hardening represented by κ, which evolves to account for the storage and annihilation of statistically stored dislocations. The Macaulay bracket dictates that there is no plastic flow for

$$\frac{\sqrt{\frac{3}{2}}\|\boldsymbol{\xi}\|}{1-\phi} < Y(\theta)+\kappa. \tag{2.45}$$

$V(\theta)$ determines the magnitude of the strain-rate sensitivity of yield stress at higher strain rates, while $\dot{\epsilon}_0(\theta)$ is the transition strain-rate from rate-insensitive to rate-sensitive yield. The model is tailored to specific metals by specifying the functions of temperature $\dot{\epsilon}_0(\theta)$, $Y(\theta)$, and $V(\theta)$, and the state variable evolution equations $\dot{\phi}$, $\dot{\kappa}$, and $\dot{\boldsymbol{\alpha}}$.

The Jaumann rate of the back stress

$$\mathring{\boldsymbol{\alpha}} = h(\theta)\,\mathbf{d}^p - \left[\sqrt{\frac{2}{3}}r_d(\theta)\,||\mathbf{d}^p|| + r_s(\theta)\right]\sqrt{\frac{2}{3}}||\boldsymbol{\alpha}||\boldsymbol{\alpha} \tag{2.46}$$

is expressed in terms of a competition between hardening $h(\theta)$ and mechanisms of recovery $r_d(\theta)$ and $r_s(\theta)$, as is the evolution of the isotropic hardening

$$\dot{\kappa} = \sqrt{\frac{2}{3}}H(\theta)\,||\mathbf{d}^p|| - \left[\sqrt{\frac{2}{3}}R_d(\theta)\,||\mathbf{d}^p|| + R_s(\theta)\right]\kappa^2, \tag{2.47}$$

where $H(\theta)$ represents hardening while $R_d(\theta)$ and $R_s(\theta)$ are mechanisms of recovery. All these mechanisms are described by the temperature-dependent functions

$$V(\theta) = c_1 e^{-\frac{c_2}{\theta}}, \tag{2.48}$$

$$Y(\theta) = \frac{c_3}{c_{21} + e^{-\frac{c_4}{\theta}}}, \tag{2.49}$$

$$\dot{\epsilon}_0(\theta) = c_5 e^{-\frac{c_6}{\theta}}, \tag{2.50}$$

$$r_d(\theta) = c_7 e^{-\frac{c_8}{\theta}}, \tag{2.51}$$

$$h(\theta) = c_9 - c_{10}\theta, \tag{2.52}$$

$$r_s(\theta) = c_{11} e^{-\frac{c_{12}}{\theta}}, \tag{2.53}$$

$$R_d(\theta) = c_{13} e^{-\frac{c_{17}}{\theta}}, \tag{2.54}$$

$$H(\theta) = c_{15} - c_{16}\theta, \tag{2.55}$$

$$R_s(\theta) = c_{17} e^{-\frac{c_{18}}{\theta}}. \tag{2.56}$$

Finally, the model employs the damage evolution relation proposed by Cocks and Ashby [3]

$$\dot{\phi} = ||\mathbf{d}^p|| \sinh\left[\frac{2(2m-1)}{2m+1}\frac{\frac{1}{3}\langle \mathrm{tr}\sigma\rangle}{\sqrt{\frac{2}{3}}||\boldsymbol{\xi}||}\right]\frac{1-(1-\phi)^{m+1}}{(1-\phi)^m}, \tag{2.57}$$

which is driven by the level of stress triaxiality. The model has been fitted to the experimentally determined response of a number of metals. For the simulations in this study, we use the model parameters for 6061-T6 aluminum shown in Table 2.1.

The goals in developing cohesive relations which are complementary to this bulk model are to incorporate the same deformation mechanisms for which a wealth of model parameters have already been determined, covering a wide range of temperature and strain rates. In addition, the relations should incorporate the state variables $\{\phi, \kappa, \boldsymbol{\alpha}\}$ which will endow the cohesive relations with information about the deformation history of the material before the point at which bifurcation occurred.

2.3.2 Creep model

The first cohesive relations we present incorporate a simplified description of plastic flow that allows us to validate the integration algorithm described in Section 2.2, to demonstrate how cohesive models can be constructed to display specific, mechanism-based behavior, and to describe the effect of parameters in the relations. As a first approximation, we assume that once the zone has initiated, the response will be dominated by the accelerated evolution of ϕ and ϕ^* and that the other state variables are not evolving, meaning

$$\dot{\kappa} = 0 \qquad \text{and} \qquad \dot{\boldsymbol{\alpha}} = 0. \tag{2.58}$$

Table 2.1: BCJ model parameters for 6061-T6 aluminum

parameter	value	units
E	6.912×10^4	MPa
ν	$\frac{1}{3}$	unitless
c_1	0	MPa
c_2	0	K
c_3	1.59958×10^2	MPa
c_4	1.61667×10^2	K
c_5	1	s^{-1}
c_6	0	K
c_7	1.9145	MPa^{-1}
c_8	6.9444×10^2	K
c_9	1.02732×10^3	MPa
c_{10}	0	$MPa\,K^{-1}$
c_{11}	0	$MPa^{-1}s^{-1}$
c_{12}	0	K
c_{13}	4.42365×10^{-2}	MPa^{-1}
c_{14}	8.55556×10^2	K
c_{15}	8.34266×10^1	MPa
c_{16}	0	$MPa\,K^{-1}$
c_{17}	0	$MPa^{-1}s^{-1}$
c_{18}	0	K
c_{19}	0	K^{-1}
c_{20}	0	K
c_{21}	0	unitless
m	4.2	unitless

Moreover, the kinematic hardening is neglected although the back stress $\boldsymbol{\alpha}$ could be resolved onto the plane on which the cohesive zone initiates. In this simplified model, the shear response is given by

$$\dot{\Delta}_t = w_0 \dot{\epsilon}_0(\theta) \sinh\left[\frac{T_t}{\kappa\,(1-\phi^*)}\right], \tag{2.59}$$

where motivated by the associated bulk model described in Section 2.3.1, $\dot{\epsilon}_0(\theta)$ defines the strain rate at which the yield stress becomes rate-dependent, κ is the hardness, and ϕ^* is the irreversible void volume fraction which acts to magnify the stress on the remaining ligaments in the process zone. The normal opening $\dot{\Delta}_n$ is define by (2.35) from geometric arguments. The description of the response of the cohesive zone is completed by defining the evolution of the void volume fraction as

$$\dot{\phi} = \dot{\epsilon}_0(\theta) \sinh\left[\frac{T_n + |T_t|}{\kappa\,(1-\phi^*)}\right], \tag{2.60}$$

which evolves reversibly as a function of both the normal and shear traction acting on the zone. At initiation, ϕ and the hardness κ from the surrounding material are used to initialize the state of the material within the zone.

In summary, the response of the zone is given by (2.35) and (2.59), and the state variable evolution relations (2.60) and (2.36). The traction integration scheme in Section 2.2 is used to define the evolution from $\{\phi_n, \phi_n^*\}$ at time t_n to $\{\mathbf{T}_{n+1}, \phi_{n+1}, \phi_{n+1}^*\}$ at time t_{n+1} driven by the opening displacement $\boldsymbol{\Delta}_{n+1}$. The model described in this section introduces just two additional parameters, w_0 and ϕ_{init} over the parameters of the associated bulk constitutive model. In fitting the model to a particular material, we could estimate the initial width of the localized zone based on the SEM micrographs. The void volume fraction at which deformation becomes localized ϕ_{init} does not appear in the traction evolution equations; however, it does appear in the thermal conductivity (2.42). The effect of this parameter will be studied with examples in the following section.

Cohesive zone response

The response of the cohesive relations given in the previous section depends strongly on the loading history as well as the model parameters. In this section, we highlight the effect of model parameters and loading conditions on the response of the model. In all the examples that follow, the temperature-dependent changes in properties due to heating are neglected. Figure 2.2(a) shows the effect of varying ϕ_{init} over a range from 0.02 to 0.2 for a prescribed normal opening rate $\dot{\Delta}_n / (w_0 \dot{\epsilon}_0) = 0.1$. The figure shows that the magnitude of the normal traction T_n decreases as the zone is initiated at more highly damaged states. Figure 2.2(b) shows that the amount of energy dissipated in the process zone decreases as ϕ_{init} increases. This result does not mean that the total fracture energy, a combination of dissipation both inside and around the zone, decreases for higher values of ϕ_{init}. A study of boundary value problems is required to see how the overall fracture energy is affected by this parameter.

Figure 2.3 shows how the normal traction and total dissipated energy vary with prescribed normal opening rate over $0.0125 < \dot{\Delta}_n / (w_0 \dot{\epsilon}_0) < 0.8$ for $\dot{\Delta}_t = 0$ and $\phi_{\text{init}} = 0.05$. This figure

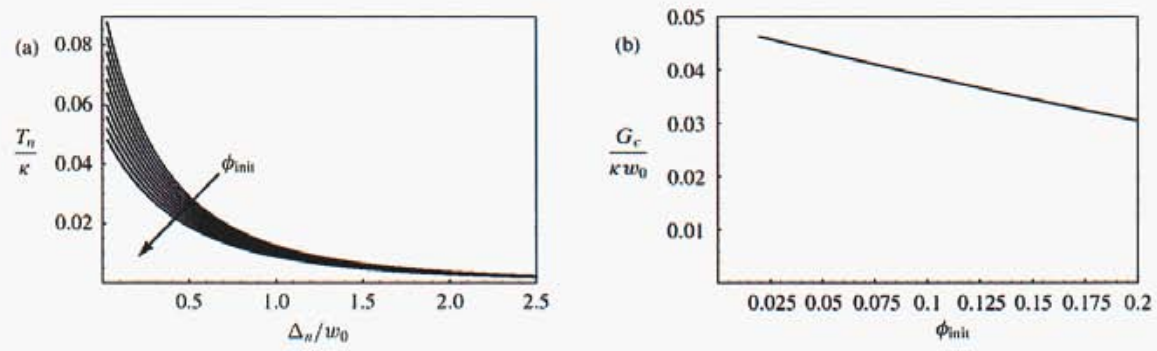

Figure 2.2: Response of the cohesive model with varying ϕ_{init} with $\dot{\Delta}_n / (w_0 \dot{\epsilon}_0) = 0.1$.

highlights the rate-dependence of the cohesive zone model. The results show that the magnitude

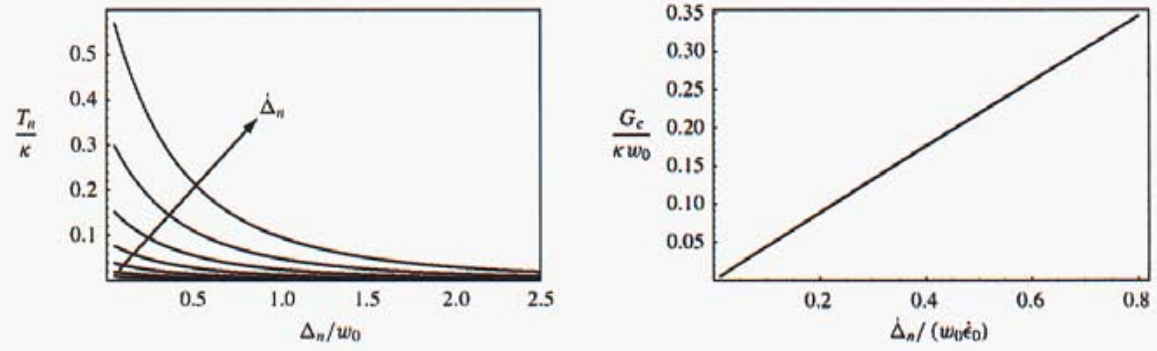

Figure 2.3: Response of the cohesive model with varying normal opening rate $\dot{\Delta}_n$ for $\dot{\Delta}_t = 0$ and $\phi_{\text{init}} = 0.05$.

of the traction and the total energy dissipated in the zone depend very strongly on the rate of opening, with the zone providing more dissipation at higher rates of deformation. In a full thermo-mechanical boundary value problem, this effect would be reduced due to a reduction in flow stress from localized heat generation and the subsequent temperature rise.

Figure 2.4 shows the response of the model subject to cyclic shear opening

$$\frac{\Delta_t}{w_0}(t) = \frac{1}{2}\left(1 - \cos\left(t/10\right)\right), \tag{2.61}$$

while maintaining $\Delta_n = 0$ with $\phi_{\text{init}} = 0.05$. For these results, the void evolution in the process zone is assumed to be fully reversible, that is $\dot{\phi}^* = \dot{\phi}$, which is evident in the figure because the magnitude of the traction is not decaying within the cycle of loading shown. These results highlight the shear-normal coupling of the model. The form of (2.60) results in dilatant response

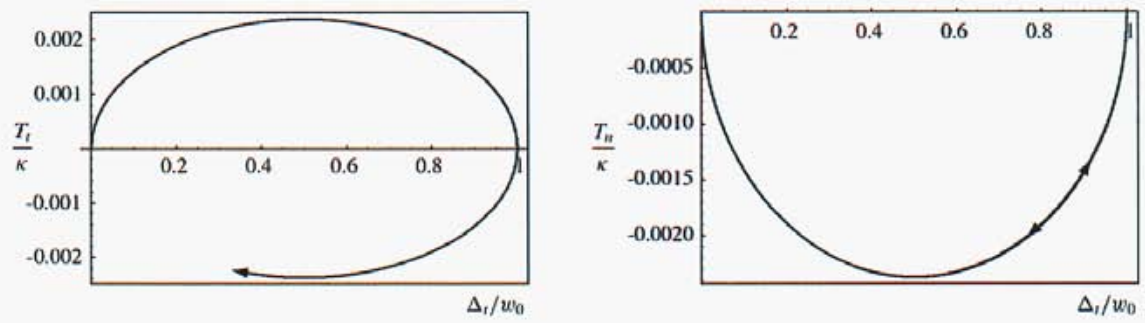

Figure 2.4: Response of the cohesive model subject cyclic opening in pure shear with reversible damage.

of the zone when subject to shear loading. For the results in figure 2.4, the opening displacement is constrained; therefore, compressive tractions are generated within the zone. In the absence of this constraint, the zone would expand in normal direction in response to the shear deformation.

Figure 2.5 shows the response of the model subject to cyclic normal opening

$$\frac{\Delta_n}{w_0}(t) = \frac{1}{2}\left(1 - \cos\left(t/10\right)\right), \tag{2.62}$$

assuming the damage in the zone to be completely irreversible, as given by (2.36). The permanent

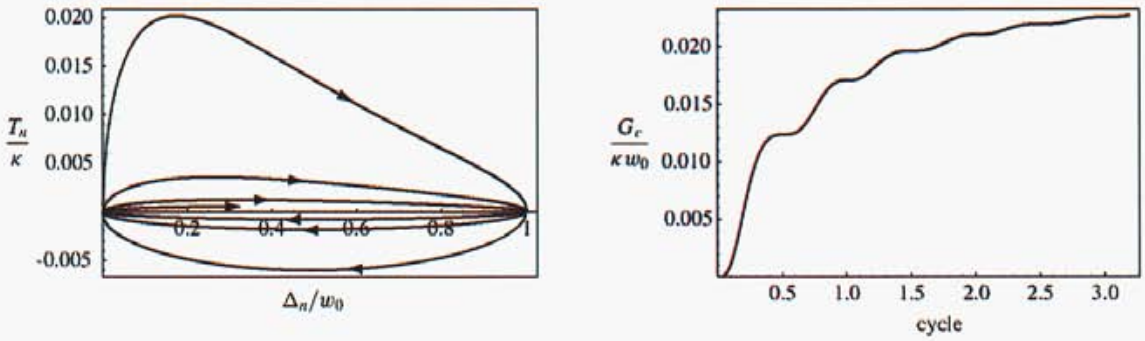

Figure 2.5: Response of the cohesive model subject cyclic opening with irreversible damage.

damage evolving in the zone is evident from the reduction in the magnitude of the traction with each cycle. The plot of dissipated energy G with each cycle is also approaching a plateau. These results highlight how degradation in the zone may accumulate at levels of traction well below those generated by rapid monotonic opening, as shown in figure 2.3.

Figure 2.6 shows the response of the model subject to cyclic loading for the case in which the void growth in the zone is assumed to be entirely reversible. As we would expect, the curves of the traction as function of the opening displacement repeatedly trace the same contour. The slight

error in successive repetitions around the contour is due to errors from the integration scheme and decreases if the time step is reduced. The evolution of damage is reversible, but dissipative both as it increases and decreases, as is evident in the plot of the work dissipated by the zone with each cycle of deformation.

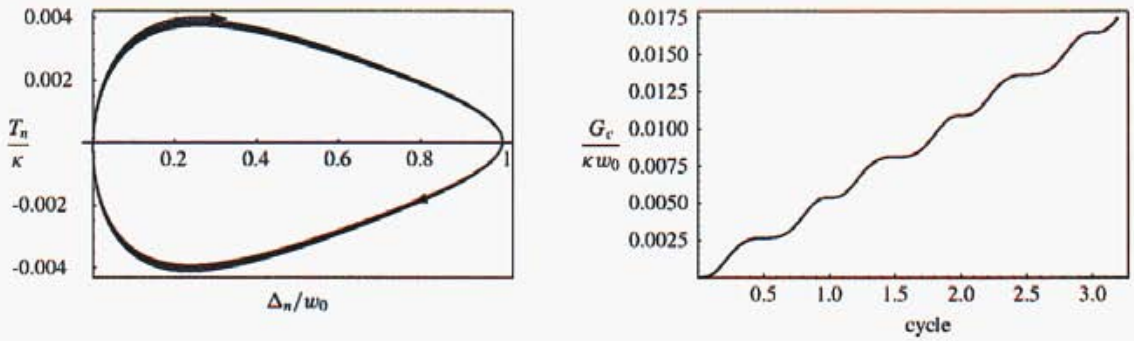

Figure 2.6: Response of the cohesive model subject cyclic opening with reversible damage.

Time-continuity of tractions

The potential for numerical artifacts in the simulation of fracture phenomena using cohesive relations that display an initially rigid response was noted by Klein *et al.* [12], demonstrated in a numerical study by Falk *et al.* [6], and analyzed mathematically in the work of Papoulia *et al.* [15]. The essential difficulty with cohesive models that display initially rigid response is illustrated in Figure 2.7. At the point of material bifurcation, the tractions acting across the surface of an im-

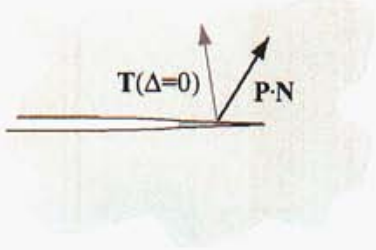

Figure 2.7: A time discontinuity in the traction at the activation of an initially rigid cohesive zone which replaces the traction $\mathbf{T} = \mathbf{PN}$ in the body with the traction $\mathbf{T}(\boldsymbol{\Delta} = 0)$ defined by the cohesive relations.

pending discontinuity is $\mathbf{T} = \mathbf{PN}$. Unless the initial response of the cohesive zone reproduces this traction

$$\mathbf{T}(\boldsymbol{\Delta} = 0) = \mathbf{PN}, \tag{2.63}$$

the activation of the cohesive zone will produce a stress shock

$$\dot{\mathbf{T}} = \frac{1}{\Delta t}\left(\mathbf{T}(\boldsymbol{\Delta} = 0) - \mathbf{PN}\right) \tag{2.64}$$

with an intensity that grows as the time step for simulation is decreased. As a result, the fracture behavior predicted by the numerical simulations fails to converge with refinement of the time step [15]. To ensure traction continuity, one could construct cohesive relations of the form

$$\mathbf{T}(\boldsymbol{\Delta}) = \mathbf{D}(\boldsymbol{\Delta})\,\mathbf{T}_0, \tag{2.65}$$

where $\mathbf{T}_0$ is the traction at initiation of the zone, and $\mathbf{D}(\boldsymbol{\Delta})$ represents a general mixed-mode evolution relation for the traction, restricted by the conditions that

$$\mathbf{D}(\mathbf{0}) = \mathbf{1} \qquad \text{and} \qquad \lim_{||\boldsymbol{\Delta}||\to\infty} \mathbf{D}(\boldsymbol{\Delta}) = \mathbf{0}. \tag{2.66}$$

The challenge then becomes embedding mechanism-based response in $\mathbf{D}$.

Due to the lack of any elastic response on the cohesive zone model and the viscous nature of the evolution equations, the cohesive relations defined by (2.35), (2.59), and (2.60) guarantee that the tractions on the surface across which a cohesive zone is introduced remain continuous in time. We can understand why the tractions remain continuous in time by noting that the strains in the body surrounding the zone, and therefore the stresses, remain continuous in time as long as the opening displacement in the zone is continuous. The requirement for continuous opening displacements implies boundedness for the rate equations (2.35), (2.59), and (2.60). Indeed, the evolution equations yield bounded values for $\dot{\Delta}_t$, $\dot{\Delta}_n$, and $\dot{\phi}$ for all bounded values of $\mathbf{T}$ as long as $\phi \neq 1$, which is certainly true when the cohesive zone begins to evolve.

To demonstrate the time-continuity of traction, we calculate the evolution of stresses with a system composed of two elastic elements bound by a cohesive layer, as shown in Figure 2.8(a). The system is loaded by prescribing displacements for the nodes on the upper surface

$$\frac{\boldsymbol{\delta}}{w_0}(\hat{t}) = \begin{Bmatrix} 0.2 \\ 1 \end{Bmatrix} \hat{t}, \tag{2.67}$$

where $\hat{t} = t\dot{\epsilon}_0$. Since the bulk model for this demonstration is elastic, we define the response of the interface as

$$\dot{\boldsymbol{\Delta}} = \begin{cases} 0 & \text{for} \quad \hat{t} \leq 1, \\ \dot{\boldsymbol{\Delta}}(\mathbf{T}, \phi, \phi^*) & \text{for} \quad \hat{t} > 1, \end{cases} \tag{2.68}$$

which dictates that the interface remains rigid until time $\hat{t}$ after which the opening evolves as dictated by the stresses acting on the cohesive zone. The results shown in Figures 2.8 (b), (c), and (d) show that although the stress evolves rapidly once the zone is activated, all three components of the stress remain continuous in time.

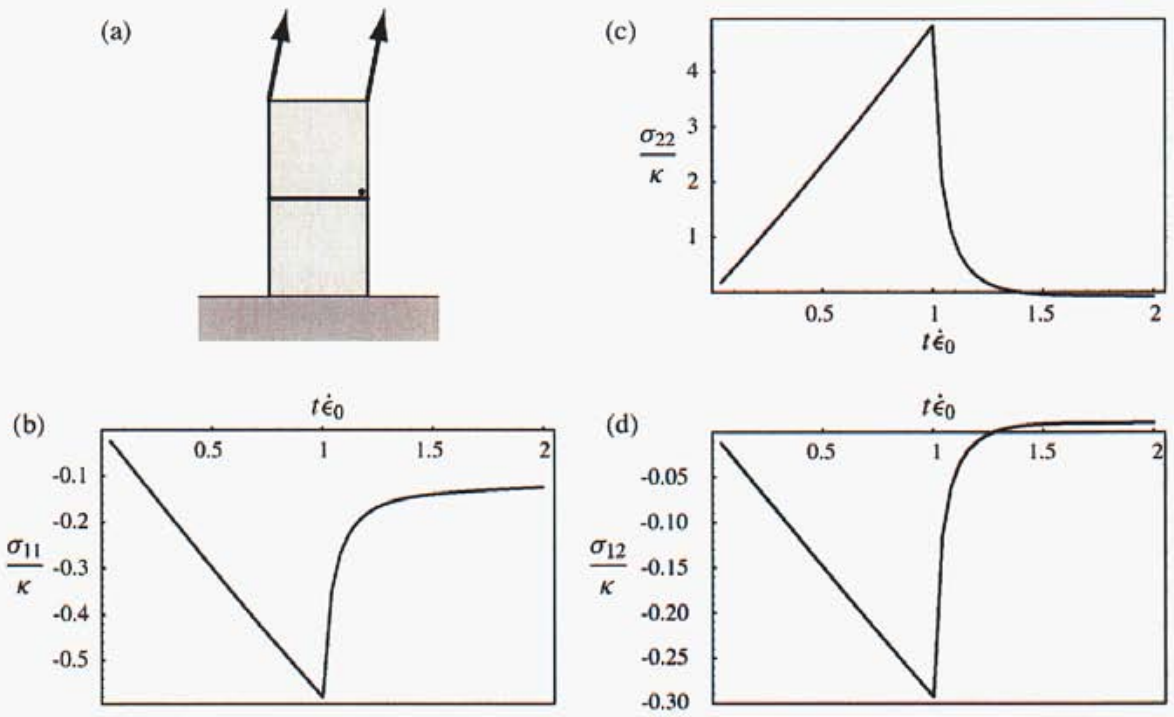

Figure 2.8: Continuous time evolution of the stresses at the point shown in (a) of the components (b) σ_{11}, (c) σ_{22}, and (d) σ_{12}.

2.3.3 Yield-point model

Since the motion of thermally activated dislocations becomes negligibly small in metals at room temperature as the stress decreases, we would like to develop cohesive zone relations that display yield-point behavior. Unlike a creep model, the mechanisms of inelastic deformation remain frozen below some critical stress. The addition of yield-point behavior complicates the formulation and implementation of the cohesive zone relations because they can arbitrarily switch between playing the role of constraints and evolution equations. In this section, we develop mixed-mode cohesive relations that respond rigidly when subject to insufficient driving tractions. We also formulate the enforcement of displacement constraints when rigid response is predicted.

Following the general structure of cohesive zone relations described in Section 2.3, we define the damage evolution and shear opening evolution equations as

$$\dot{\Delta}_t = \phi w_0 \dot{\epsilon}_0(\theta) \sinh\left[\frac{1}{V(\theta)}\left\langle \frac{|T_t|}{(1-\phi^*)^m} - (Y(\theta)+\kappa)\right\rangle\right]\frac{T_t}{|T_t|} \tag{2.69}$$

and

$$\dot{\phi} = \phi \dot{\epsilon}_0(\theta) \sinh\left[\frac{1}{V(\theta)}\left\langle \frac{|\hat{T}|}{(1-\phi^*)^m} - (Y(\theta)+\kappa)\right\rangle\right]\frac{\hat{T}}{|\hat{T}|}, \tag{2.70}$$

respectively. Once again, we assume $\dot{\kappa} = 0$ and $\dot{\alpha} = 0$ within the zone. The evolution for the normal opening displacement $\dot{\Delta}_n$ (2.35) is determined entirely by geometric considerations. The driving force for the evolution of the shear opening displacement is T_t, while a mixed-mode, effective stress

$$\hat{T} = T_n + |T_t| \tag{2.71}$$

is defined as the driving force for damage evolution. The form of $\hat{T}$ in (2.71) indicates that damage evolution is accelerated under tensile loading ($T_n > 0$) in the presence of shear stress. Conversely, damage evolution is retarded under shear loading in the presence of compressive stress ($T_n < 0$). The yield-point behavior is introduced in $\dot{\phi}$ and $\dot{\Delta}_t$ through the Macauley bracket

$$\langle x \rangle = \begin{cases} x & \text{for} \quad x > 0, \\ 0 & \text{for} \quad x \leq 0, \end{cases} \tag{2.72}$$

indicating that the evolution equations remain frozen if the driving stress, magnified by $(1-\phi^*)^{-m}$ due to the presence of damage, does not exceed the flow stress $Y(\theta) + \kappa$, where $Y(\theta)$ is the temperature-dependent initial yield stress and κ is the additional hardness resulting from the accumulation of statistically stored dislocations. $V(\theta)$ determines the rate dependence of the flow stress. This rate-dependence can be better understood by inverting either (2.69) or (2.70) to isolate the associated driving stress, assuming the yield point has been reached. From (2.69), we find

$$|T_t| = \left(1-\phi^*\right)^m \left[V(\theta) \sinh^{-1}\left(\frac{\dot{\Delta}_t}{\phi\, w_0\, \dot{\epsilon}_0(\theta)} \right) + \left(Y(\theta) + \kappa\right) \right], \tag{2.73}$$

where T_t is assumed to be positive. The relation (2.73) indicates that the flow stress approaches $(1-\phi^*)^m\,(Y(\theta)+\kappa)$ at very small opening rates ($|\dot{\Delta}_t| \ll \phi\, w_0\, \dot{\epsilon}_0(\theta)$), while $V(\theta)$ becomes more influential as the opening rate increases.

The form of the evolution equations ensures that any possible solutions for the tractions $\{T_t, T_n\}$, computed by the traction integration scheme described in Section 2.2, can be determined for all opening rates $\{\dot{\Delta}_t, \dot{\Delta}_n\}$ over the interval $\phi \in [0, 1)$. This character of the evolution equations can be seen by noting that the evolution rates $\{\dot{\Delta}_t, \dot{\Delta}_n, \dot{\phi}\}$ all vanish for any traction $\{T_t, T_n\}$ as $\phi \to 0$ and diverge for any traction as $\phi \to 1$. As a result, the problem of integrating the tractions can be stabilized by scaling the updates to the local unknowns such that ϕ does not change too rapidly between iterates and remains within the admissible bounds.

The material's inability to sustain loads as it approaches complete failure corresponds to the diverging evolution rates for any applied traction as $\phi \to 1$. However, vanishing tractions with increasing opening displacements are not sufficient to guarantee that the cohesive model will exhibit a finite work to fracture. Restricting the deformation to normal opening ($\dot{\Delta}_t = 0$), we can apply a change of variables to (2.32) using (2.35) to express the work to fracture as

$$G_c = \lim_{\Delta_n \to \infty} \int_0^{\Delta_n} T_n(\Delta')\, d\Delta' = \lim_{\phi \to 1} \int_0^{\phi} \frac{T_n\, w_0}{(1-\phi')^2}\, d\phi'. \tag{2.74}$$

Inverting (2.70) with (2.35) to recover T_n, we can express a representative work to fracture as

$$G_c^* = \lim_{\phi \to 1} \int_0^{\phi} w_0 \left(1 - \phi'\right)^{m-2} \left[V \sinh^{-1} \left(\frac{\dot{\Delta}_n \left(1 - \phi'\right)^2}{\phi' w_0 \dot{\epsilon}_0} \right) + (Y + \kappa) \right] d\phi', \tag{2.75}$$

for the dissipation under conditions of growth for which ϕ increases monotonically, so that $\phi^* = \phi$, the opening is strictly normal ($\dot{\Delta}_t = 0$ and $T_t = 0$), and the normal opening rate $\dot{\Delta}_n$ remains constant. We would expect all these conditions, except the condition for constant $\dot{\Delta}_n$, to be satisfied for monotonic, mode I crack growth. Despite this restriction, the dissipation given by (2.75) is useful for assessing the effects of the parameters in the model, and for determining conditions under which the dissipation is finite. One approach to ensuring finite dissipation is to avoid the singularity at $\phi = 1$ by limiting the upper bound of ϕ at some $\phi_{\max} < 1$. This modification imposes a cut-off on the response of the model above which $T_n = 0$. In evaluating the limit in (2.75), we note that the term in the integrand involving $\sinh^{-1}$ is less singular than the second term involving $(Y + \kappa)$, which are constant if we neglect changes in Y with temperature. From this observation, we require

$$(1 - \phi)^{m-2} < (1 - \phi)^{-1} \tag{2.76}$$

in order to ensure the integral is bounded, from which we find the restriction that $m > 1$. This result indicates that the stress concentrating effects of damage must be at least as large as the stress magnification resulting from the reduction in the load-bearing area ($m = 1$).

The procedure described in Section 2.2 is a displacement driven algorithm for determining the updated traction and state variables when the evolution equations are active. Before the yield point is reached, the cohesive relations dictate that the opening displacements must remain constant. Under these conditions, the displacements are prescribed, while the tractions in the zone are determined by solution of the global boundary-value problem, as opposed to the local traction integration, subject to the constraints imposed by the cohesive relations.

Enforcement of rigid response in the cohesive zone is expressed in terms of constraint equations, along the normal and tangent directions, of the form

$$h_i = \Delta_i(t_{n+1}) - \Delta_i(t_n)\,, \tag{2.77}$$

such that the condition $\dot{\Delta}_i = 0$ implies $h_i = 0$. Constraints are required for the tangent and normal directions independently, as dictated by the loading conditions. A number of approaches are available for enforcing these constraints. We investigated the performance of two approaches, a penalty approach and an augmented Lagrangian method. Although each approach has its advantages, our experience indicates the augmented Lagrangian method is better suited to enforcement of the rigid conditions associated with cohesive models which display yield point behavior. The details for our findings are discussed in the sections that follow.

Penalized constraints

With penalized approaches, violation of the constraints produces an increase in the total potential of the system which is usually expressed as a quadratic potential

$$U_i = \frac{1}{2} k h_i^2, \tag{2.78}$$

where k is a regularization parameter which determines how strictly the constraint is enforced. The force resulting from enforcement of a constraint is given by

$$f_i = -\frac{\partial U_i}{\partial h_i} = -k h_i, \tag{2.79}$$

or is just proportionate to the amount that the constraint is violated. The advantage of the penalized approach is the simplicity of the formulation. Furthermore, it does not introduce any unknowns to the problem that is being constrained. The main disadvantage is that the approach only enforces constraints approximately, with stricter enforcement produced by increasing the value of k, limited by the stiffness at which the solution procedure becomes unstable. The formulation adds compliance to the system being constrained. For constraining displacements within a cohesive zone, this compliance is a problem because the characteristic opening displacements are very small. The error in the opening displacements produced by the penalized constraints can easily exceed the scale of the displacements over which the tractions evolve to complete failure. These errors can be reduced by increasing k, but for the example problems presented in Section 4, the solution procedure became unstable before the magnitude of the errors in enforcing the constraints was reduced to an acceptable level. This behavior occurs because the overall system scale is much larger than the characteristic opening displacements in the cohesive zone.

The penalized constraints are expressed separately for the tangent and opening directions as

$$U_t = \frac{1}{2} k \left([\Delta_t]_{n+1} - [\Delta_t]_n \right)^2 . \tag{2.80}$$

$$U_n = \frac{1}{2} k \left([\Delta_n]_{n+1} - [\Delta_n]_n \right)^2 . \tag{2.81}$$

where we introduce the notation $\bullet(t_n) = [\bullet]_n$ to distinguish between the subscripts representing directions and time. The tractions produced by the constraints are then

$$[T_t]_{n+1} = \frac{k}{A} \left([\Delta_t]_{n+1} - [\Delta_t]_n \right) . \tag{2.82}$$

$$[T_n]_{n+1} = \frac{k}{A} \left([\Delta_n]_{n+1} - [\Delta_n]_n \right) . \tag{2.83}$$

where A is the tributary area associated with the constrained point. Note that when the constraints are active, the tractions generated in the constrained direction are decoupled from the opening displacements in the perpendicular direction. Linearization of the zone response then depends on which of the opening displacements is constrained. For the evolution equations given by (2.69)

and (2.70), we note $\frac{\partial \dot{\boldsymbol{\Delta}}}{\partial \boldsymbol{\Delta}} = 0$ which allows the incremental response of the zone model (2.30) to be simplified as

$$d\boldsymbol{\Delta}_{n+1} = \Delta t \left[\frac{\partial \dot{\boldsymbol{\Delta}}}{\partial \mathbf{T}} + \frac{\partial \dot{\boldsymbol{\Delta}}}{\partial \mathbf{q}} \left(\frac{1}{\Delta t} \mathbf{1} - \frac{\partial \dot{\mathbf{q}}}{\partial \mathbf{q}} \right)^{-1} \frac{\partial \dot{\mathbf{q}}}{\partial \mathbf{T}} \right] d\mathbf{T}_{n+1}, \tag{2.84}$$

which we rewrite as

$$\begin{Bmatrix} d\Delta_t \\ d\Delta_n \end{Bmatrix}_{n+1} = \begin{bmatrix} A_{tt} & A_{tn} \\ A_{nt} & A_{nn} \end{bmatrix} \begin{Bmatrix} dT_t \\ dT_n \end{Bmatrix}_{n+1} \tag{2.85}$$

to define the components of the Jacobian matrix associated with active evolution equations. We then consider three cases:

(i) $\dot{\Delta}_t = 0$ and $\dot{\Delta}_n = 0$: For this case, constraints are active in both the tangent and normal directions. The incremental response does not involve the cohesive relations and is given by

$$d\,[T_n]_{n+1} = \frac{k}{A} d\,[\Delta_n]_{n+1}\,, \tag{2.86}$$

$$d\,[T_t]_{n+1} = \frac{k}{A} d\,[\Delta_t]_{n+1}\,. \tag{2.87}$$

(ii) $\dot{\Delta}_t = 0$ and $\dot{\Delta}_n \neq 0$: For this case, the shear opening displacement is constrained, while the normal opening evolves as dictated by the cohesive relations. The active constraint means T_t is given by (2.82) and is not treated as an unknown in the local traction integration procedure. As in case (i), the linearization of T_t yields

$$\frac{\partial\,[T_t]_{n+1}}{\partial\,[\Delta_t]_{n+1}} = \frac{k}{A} \qquad \text{and} \qquad \frac{\partial\,[T_t]_{n+1}}{\partial\,[\Delta_n]_{n+1}} = 0. \tag{2.88}$$

Including the constraint traction T_t (2.82) in linearizing the evolution of the normal traction yields

$$\frac{\partial\,[T_n]_{n+1}}{\partial\,[\Delta_n]_{n+1}} = \frac{1}{\Delta t\, A_{nn}} \qquad \text{and} \qquad \frac{\partial\,[T_n]_{n+1}}{\partial\,[\Delta_t]_{n+1}} = -\frac{k}{A}\frac{A_{nt}}{A_{nn}}. \tag{2.89}$$

(iii) $\dot{\Delta}_t \neq 0$ and $\dot{\Delta}_n = 0$: For this case, the normal opening displacement is constrained, while the shear opening evolves as dictated by the cohesive relations. Following arguments analogous to case (ii), we find

$$\frac{\partial\,[T_n]_{n+1}}{\partial\,[\Delta_t]_{n+1}} = 0 \qquad \text{and} \qquad \frac{\partial\,[T_n]_{n+1}}{\partial\,[\Delta_n]_{n+1}} = \frac{k}{A} \tag{2.90}$$

from the linearization of the normal tractions, while linearization of the shear response yields

$$\frac{\partial\,[T_t]_{n+1}}{\partial\,[\Delta_t]_{n+1}} = \frac{1}{\Delta t\, A_{tt}} \qquad \text{and} \qquad \frac{\partial\,[T_t]_{n+1}}{\partial\,[\Delta_n]_{n+1}} = -\frac{k}{A}\frac{A_{tn}}{A_{tt}}. \tag{2.91}$$

Augmented Lagrangian constraints

Unlike penalized approaches for enforcing constraints, Lagrange multiplier methods result in exact satisfaction of the constraint equations. Following the treatment of Powell [16] and Hestenes [9], the constraints are enforced by perturbing the Lagrangian functional for the system as

$$L(\mathbf{u}, \boldsymbol{\lambda}) = \int_{\Omega} W(\mathbf{F}(\mathbf{u}))\, d\Omega + \int_{\Gamma^c_{\text{int}}} \left(\boldsymbol{\lambda} \cdot \mathbf{h}(\mathbf{u}) + \frac{1}{2} r\, \mathbf{h}(\mathbf{u}) \cdot \mathbf{h}(\mathbf{u}) \right) d\Gamma, \tag{2.92}$$

where $W(\mathbf{F})$ defines the free energy of the bulk and $\boldsymbol{\lambda}$ is the field of multipliers which acts to enforce the constraints $\mathbf{h}$ over the internal surface Γ^c_{int}. The regularization parameter r does not affect the solution but its value does affect the stability of the solution procedure. Without loss of generality, we assume the surface Γ^c_{int} over which the constraints are acting is the same for all components of $\mathbf{h}$ rather than defining separate surfaces for each component. From (2.92), we can define the equations for static equilibrium

$$\int_{\Omega} \mathbf{P}{:}\delta\mathbf{F}\, d\Omega + \int_{\Gamma_{\text{int}}} \mathbf{T} \cdot \delta\boldsymbol{\Delta}\, d\Gamma + \int_{\Gamma^c_{\text{int}}} (\boldsymbol{\lambda} + r\, \mathbf{h}) \cdot \delta\mathbf{h}\, d\Gamma = \int_{\Gamma_h} \mathbf{T} \cdot \delta\mathbf{u}\, d\Gamma, \tag{2.93}$$

$$\int_{\Gamma^c_{\text{int}}} \mathbf{h} \cdot \delta\boldsymbol{\lambda}\, d\Gamma = 0, \tag{2.94}$$

where $\mathbf{P} = \frac{\partial W}{\partial \mathbf{F}}$ is the nonsymmetric 1st Piola-Kirchhoff stress, and $\mathbf{T} = \mathbf{P}\mathbf{N}$ is the force per unit undeformed area with normal $\mathbf{N}$. Kinematic boundary conditions are satisfied in the selection of functions used to represent $\mathbf{u}$, and traction boundary conditions produce the contribution to (2.93) over Γ_h. Tractions acting across internal surfaces produce the contribution over Γ_{int}, while constraints are acting over the internal surfaces Γ^c_{int}. From the equilibrium equations, we see that r does not affect the solution of (2.93) once the constraint equation (2.94) is satisfied.

Discretization of the integrals over Γ^c_{int} results in a series of discrete constraint equations that will be satisfied exactly. The difficulty with imposing exact enforcement is that the it can result in a system that is over constrained. The overconstrained condition is illustrated by the results shown in Figure 2.9(a). The figure shows the deformed configuration of a small mesh comprised of four bilinear, quadrilateral elements. The two upper elements are bound to the two lower elements by cohesive elements that lie along the midline of the mesh. Two-point Gauss integration is used to integrate the tractions over the interface elements. As indicated in the figure, the rigid constraints are enforced at both integration points of surface element 1, while only one integration point is constrained over element 2. Since the cohesive elements used in this calculation can only support linear variations in the displacement jump across the element, the partially constrained element is forced to remain closed. Moreover, the tractions enforcing the constraints, although correctly reflecting the total force transferred across the interface, oscillate wildly since the constraints act against each other. Since these tractions are used to determine whether the cohesive relations are active, their values must be well-behaved and accurate.

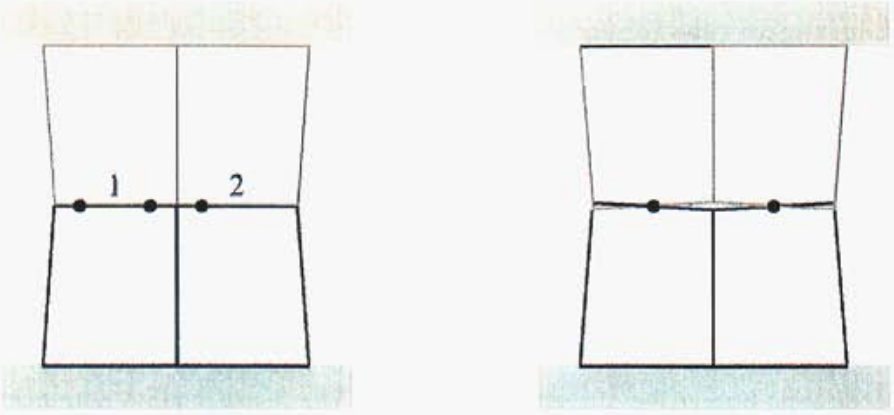

Figure 2.9: Illustration of the difficulties associated with exact enforcement of rigid response in the cohesive relations at element integration points showing (a) an overconstrained problem and (b) an underconstrained problem. The constrained points are indicated with •.

The results of attempting to reduce the number of constraints in the system is shown in Figure 2.9(b). Here the constraints are integrated using just a single integration point at the element centroid, while tractions over element without constraints are still integrated with a standard two-point Gauss integration scheme. The oscillatory profile of the surfaces indicates the system is underconstrained. Aside from the inaccuracies in the solution this approach produces at the interface due to the oscillations, using separate schemes for integrating the constraints and the tractions introduces additional errors associated with transferring traction and gap information from one set of integration points to the other. This issue is especially problematic during the solution procedure as constraints are activated and deactivated. The source of the difficulties with both of these cases is that the number of constraints does not match the number of degrees of freedom on the interface. The natural solution for avoiding problems with over or under constraint, as well as the errors associated with transferring information between integration points, is to apply a nodal integration scheme to integrate both the constraints when rigid and tractions when evolving. We define a nodal integration scheme as

$$\int_{\Gamma^c_{\text{int}}} \mathbf{h}\, d\Gamma = \sum_{I \in \mathcal{I}^+} \mathbf{h}(\mathbf{X}_I)\, A_I, \tag{2.95}$$

where $\mathcal{I}^+$ is the set of nodes on either side of the surface Γ^c_{int}. A_I is the tributary area associated with node I defined as

$$A_I = \int_{\Gamma_{\text{int}}} N_I\, d\Gamma, \tag{2.96}$$

where N_I is the shape function of node I. Using the nodal integration scheme in (2.95) to evaluate all the surface integrals over Γ_{int} and Γ^c_{int} in (2.93) and (2.94) allows smooth transitions between

evolving opening displacements and constrained states. In addition, the constraints are enforced exactly by the augmented Lagrangian formulation.

Cohesive zone response

To demonstrate the response of the cohesive model under different loading conditions and for different model parameters, we employ the same configuration illustrated in Figure 2.8(a), namely, two continuum element bound by a cohesive layer. In these calculations, each of the square elements has dimensions 0.1×0.1 mm. Some of the calculations in this section attempt to isolate the response of the cohesive zone from the behavior of the surrounding material by prescribing elastic bulk response with the elastic moduli of 6061-T6 aluminum listed in Table 2.1. Since the elastic bulk cannot provide evolving damage information to the zone to trigger initiation, we initialize the damage in the zone to $\phi_0 = \phi_{\text{init}} > 0$ and allow the zone to begin evolving as dictated by the zone traction. For the calculations which include plasticity in the bulk, all parameters listed in the table are used to define the response of the BCJ model described in Section 2.3.1 at a temperature of 297 K.

The parameters defining $\dot{\epsilon}_0(\theta)$ and $Y(\theta)$ in the cohesive relations are also taken from the values for 6061-T6 in Table 2.1. The parameters shown for 6061-T6 indicate a rate-independent initial yield stress ($V(\theta) = 0$). Since $V(\theta)$ appears in the denominator of terms within the evolution equations for the cohesive model, the rate-independent limit must be treated as a special case that we do not consider here. Instead, we specify $V(\theta) = 1$, which implies the model will exhibit rate-dependent behavior for $|\dot{\Delta}_t|, |\dot{\Delta}_n| > w_0\dot{\epsilon}_0$. The micrographs described in Section 3.4 indicate $w_0 < 5\mu$m, though accurate determination of the zone width is not available. All of the calculations are performed under quasistatic loading conditions. In principal, one could select any value of the damage evolution exponent m satisfying $m > 1$, as required for a bounded fracture energy. However, we encountered an instability in the traction evolution for $m > 1$ which is illustrated in Figure 2.10. The results show that the tractions in the zone decay smoothly once sufficient stress is applied to the zone, but that the response becomes oscillatory at some opening $\frac{\Delta_n}{w_0} > 40$. We found the magnitude of the oscillations decreased with smaller load increments, but never disappeared entirely. We found that the tractions do decay smoothly for $m = 1$, but the analysis above shows this choice produces an unbounded work to fracture due to singularities in the evolution equations for $\phi \to 1$. In order to produce a bounded work to fracture, while avoiding the oscillatory response shown in Figure 2.10, we choose $m = 1$ and define a failure damage $\phi_{\max} < 1$ which signifies the maximum amount of damage the material can sustain before complete failure, after which $\mathbf{T} = 0$. Avoiding the singularity as $\phi \to 1$ yields a bounded work to fracture at the cost of a discontinuous drop in the traction when $\phi = \phi_{\max}$.

Figure 2.11 shows the results of evaluating the expression for the representative work to fracture (2.75) over a range of opening rates $\dot{\Delta}_n$ spanning eight decades on the log scale. The results in Figure 2.11(a) are obtained by integrating (2.75) numerically assuming constant opening rates. The values are normalized by the representative fracture energy G_c^* at the rate-independent limit ($\dot{\Delta}_n \to 0$). Results from the two-element finite element calculations are shown for $\log\left[\dot{\Delta}_n / (w_0\dot{\epsilon}_0)\right] > 0$ from simulations with constant prescribed velocity $\dot{\delta}_n$ of the upper boundary. At long times,

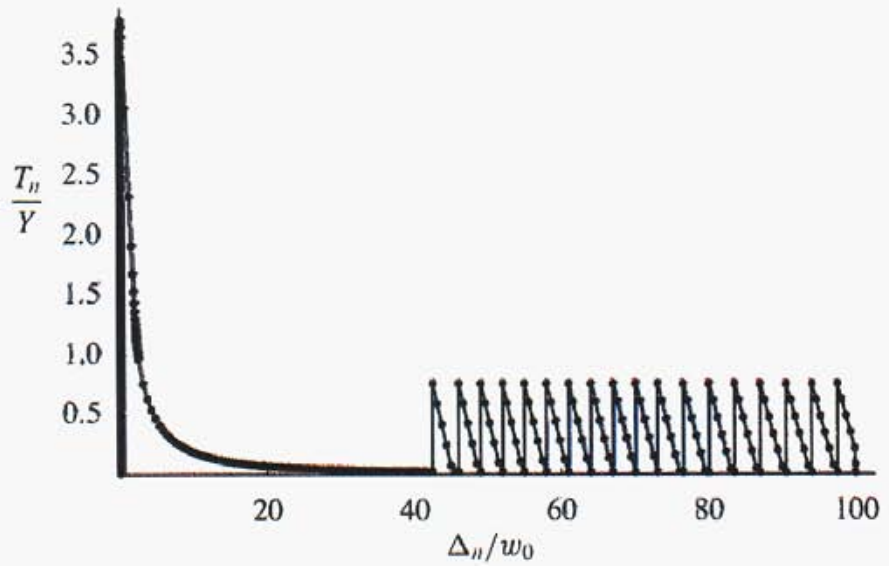

Figure 2.10: Instabilities in the traction integration for $m = 1.05$ with $\phi_{\text{init}} = 5\%$, $\dot{\Delta}_t = 0$, $w_0 = 1\ \mu\text{m}$, and $\frac{\dot{\Delta}_n}{w_0 \dot{\epsilon}_0} = 1000$.

$\dot{\delta}_n = \dot{\Delta}_n$; however $\dot{\Delta}_n$ can far exceed $\dot{\delta}_n$ at the onset of zone evolution driven by the release of stored energy in the surrounding bulk. Despite these differences, the values from the two-element calculations agree well with the values obtained by integrating (2.75).

Figure 2.12 shows the traction-separation response of the model for boundary conditions that include a load reversal. The vertical segments of the loop in the curve indicate the evolution relations have frozen, meaning that the stress, even magnified by damage, has dropped below the flow stress $Y + \kappa$. The horizontal segments of the loop indicate the cohesive zone is driven to yield in compression before being loaded again in tension. The curve shows no abrupt corners or jumps in the response which indicates the model switches smoothly between states of constraint and flow. A detailed look at the time evolution of zone is shown in Figure 2.13. The applied displacement boundary conditions are shown in Figure 2.13(a). Ramps of $\frac{\dot{\delta}}{w_0 \dot{\epsilon}_0} = \pm 1000$ first stretch the zone, then compress it before stretching it again. Figure 2.13(b) shows the traction evolving smoothly through multiple transitions between states of constraint and flow, with yielding occurring in both tension and compression. Figure 2.13(c) illustrates how the zone remains closed until approximately t = 20, when the traction in the zone reaches a sufficiently high level. Two additional horizontal segments in the curve indicate other periods of rigid response. Figure 2.13(d) highlights the difference in evolution between the void volume fraction ϕ, which is kinematically linked to the normal opening displacement through (2.35) and ϕ^*, which stores the material's memory of the maximum damaged state.

In the calculations shown thus far, an elastic bulk model is used to isolate the response of the dissipation mechanisms in the cohesive relations from any in the bulk. The damage in the zone was

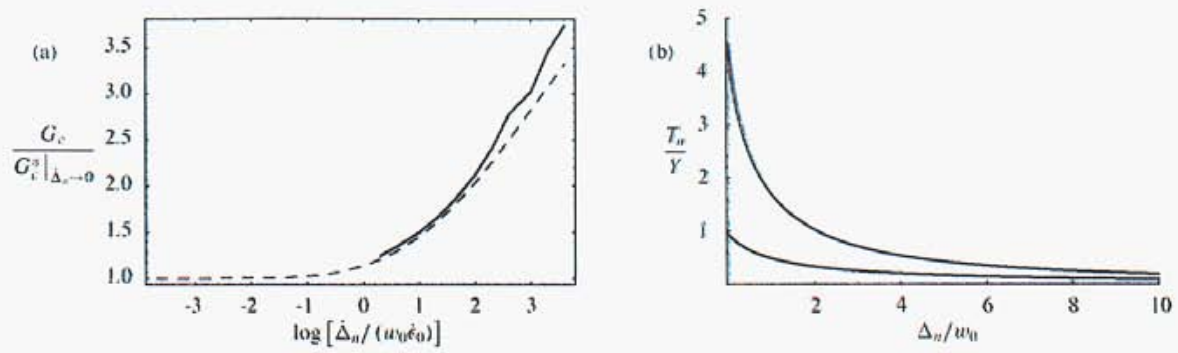

Figure 2.11: (a) variation in the fracture energy as a function of the opening rate $\dot{\Delta}_n$ from (2.75) (dashed line), compared with finite element calculations results (solid line) for $\log\left[\dot{\Delta}_n/(w_0\dot{\epsilon}_0)\right] > 0$, and (b) the difference in the traction-separation response for $\log\left[\dot{\Delta}_n/(w_0\dot{\epsilon}_0)\right] = -3$ and 3, corresponding to the lower and upper curves, respectively.

initialized to different values of ϕ_{init}, and flow occurred when the traction reached a sufficiently high level. In this final example shown in Figure 2.14, the BCJ model is used for the bulk. Before the damage in the zone reaches the value which triggers the opening of the zone ($\phi < \phi_{\text{init}}$), the damage and other state variables in the zone are updated from the nodal values computed by extrapolation from the integration points over the bulk elements. Once the damage reaches ϕ_{init}, evolution of the damage and other state variables are governed by the evolution relations of the zone itself. The figure highlights how the evolution of damage accelerates rapidly with accumulation of damage. In principal, activation of the cohesive zone should halt damage evolution in the bulk since unloading of the bulk then occurs. For larger values of ϕ_{init}, we observed that it is possible for the zone to unload slowly enough that the bulk elements are driven to a localized state. For this reason, we "freeze" the damage evolution in the bulk when $\phi > 2\phi_{\text{init}}$.

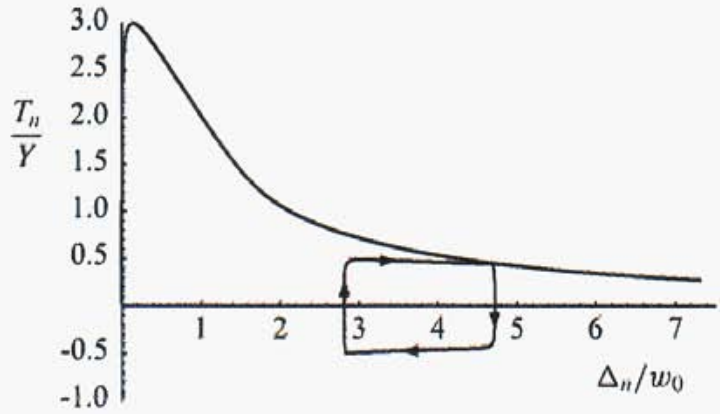

Figure 2.12: The traction-separation response of the model subject to a single load reversal with $w_0 = 1\ \mu$m with the boundary conditions shown in Figure 2.13.

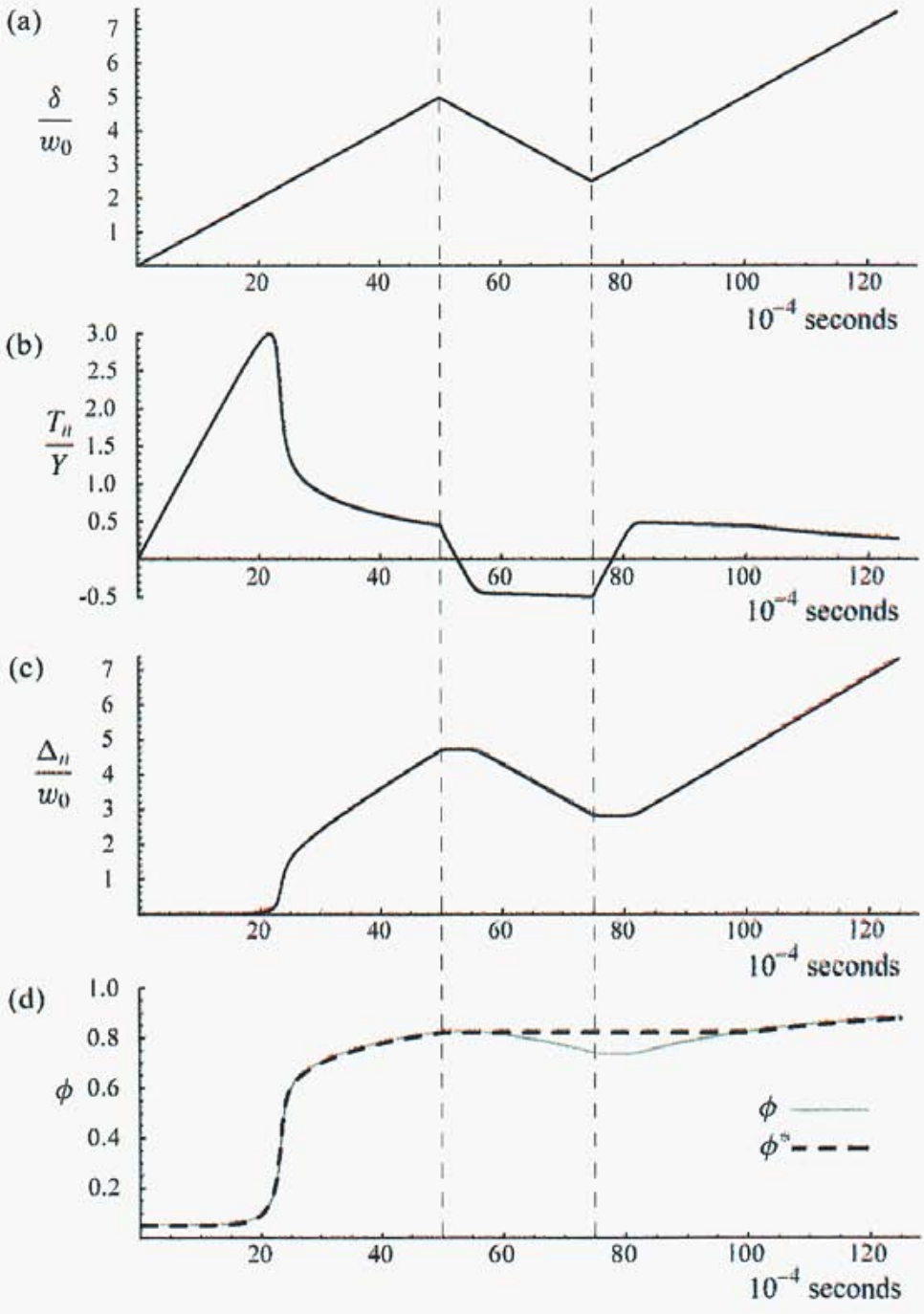

Figure 2.13: The response of the cohesive zone during a load reversal defined by the boundary conditions shown in (a), where $\frac{\dot{\delta}}{w_0 \dot{\epsilon}_0} = \pm 1000$, showing the variation in (b) traction, (c) opening displacement, and (d) damage.

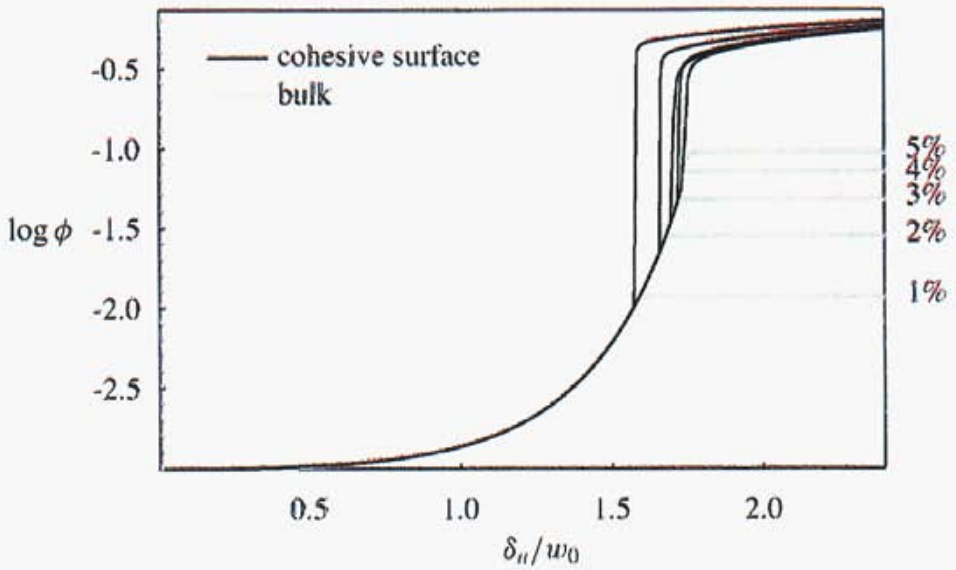

Figure 2.14: Curves showing damage evolution in the zone both before and after $\phi = \phi_{\text{init}}$, for $\phi_{\text{init}} = \{1, 2, 3, 4, 5\}$ %. Activation of the zone is indicated by the sharp jump in the zone damage, after which the bulk damage remains relatively constant.

Chapter 3

Validation experiments

3.1 *in situ* SEM straining

3.1.1 Experimental details

Specimens of annealed 304L stainless steel and 6061-T651 aluminum were prepared for three-point bend fracture experiments while observing the crack tip in a scanning electron microscope (SEM). The objective of the SEM straining experiments was to provide insight into the development of plastic zones and crack propagation. Because the straining stage load capacity was 400 lbf and because there was limited space in the SEM chamber, specimen dimensions were limited to $0.25 \times 0.25 \times 2.5$ in. The specimen size was also limited by modeling constraints. It was recognized that the small samples would not produce valid plane strain fracture toughness values from the standpoint of single value elastic-plastic fracture toughness material properties. It was also recognized that the SEM experiments would only provide information about the surface effects of fracture. However, the experiments provided both insight and load-displacement data for model comparison.

Specimens were extracted from compact tension (CT) samples using electro-discharge machining after the larger samples had been precracked using standard fracture mechanics testing procedures. Closed loop control of the servo-hydraulic test frame allowed load shedding such that the final maximum stress intensity was below 20 MPa$\sqrt{\text{m}}$ for 6061 aluminum samples and 30 MPa$\sqrt{\text{m}}$ for 304L stainless steel samples. Figure 3.1 shows a CT sample setup for precracking. Two 304L CT samples were loaded monotonically after precracking and prior to three-point bend specimen extraction, to initiate plastic zone development under the conditions of greater plastic constraint provided by the CT geometry and dimensions. In addition, side grooves were machined into some of the samples to provide constraint. After extraction, one surface of each three-point bend sample was polished. Side grooves were polished by hand. A Jeol 840 SEM fitted with a Jeol SM-TS40 straining stage, shown in Figure 3.2, was used to image the specimens while applying load.

Load-line displacement was measured with a linear variable differential transformer (LVDT) in contact with the end of the load train. A correction for machine compliance was obtained by

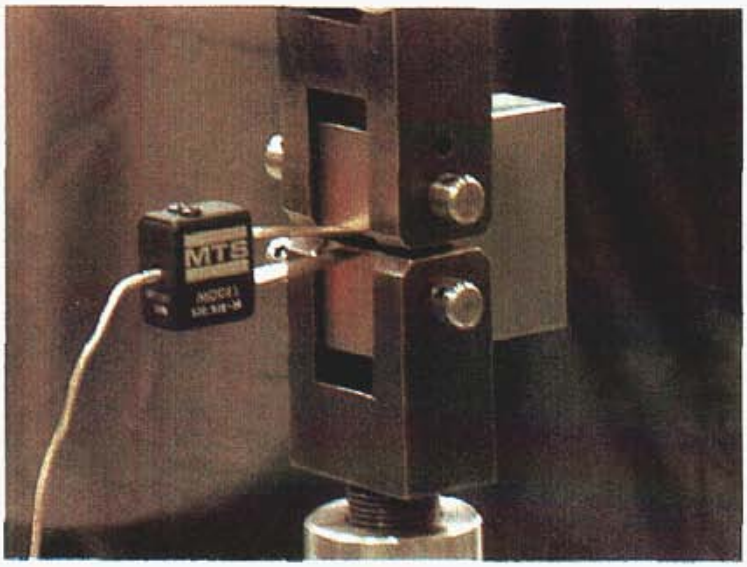

Figure 3.1: Compact tension sample setup for precracking. The clip gage provided displacement data used to calculate the fatigue crack length from specimen compliance.

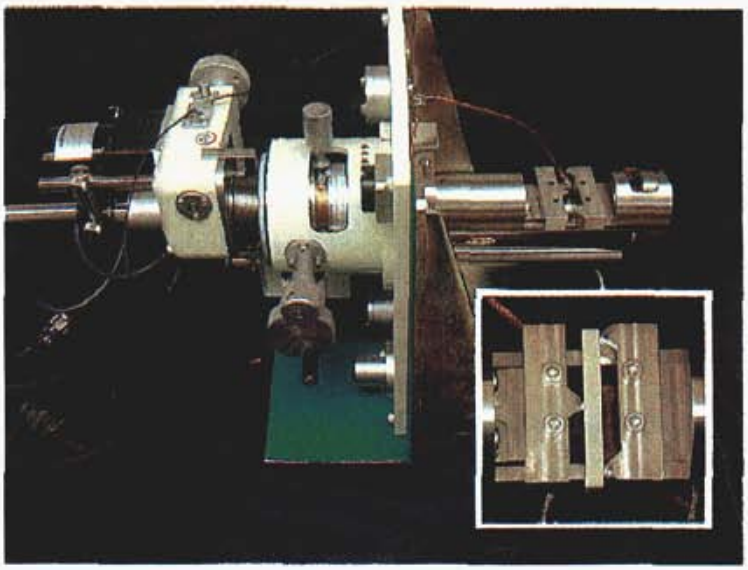

Figure 3.2: Loading stage that was used in the SEM experiments. The inset image shows a three-point bend specimen loaded in the fixture.

measuring displacement and load with a very stiff link in place of a specimen. Most of the SEM *in situ* bending tests were carried out in pure mode I loading, where the load-line was applied directly opposite the crack, and centered between the two reaction pins. However, some mixed-mode loading was performed by shifting the crack away from the load-line and shifting the load-line off center, as shown in Figure 3.3.

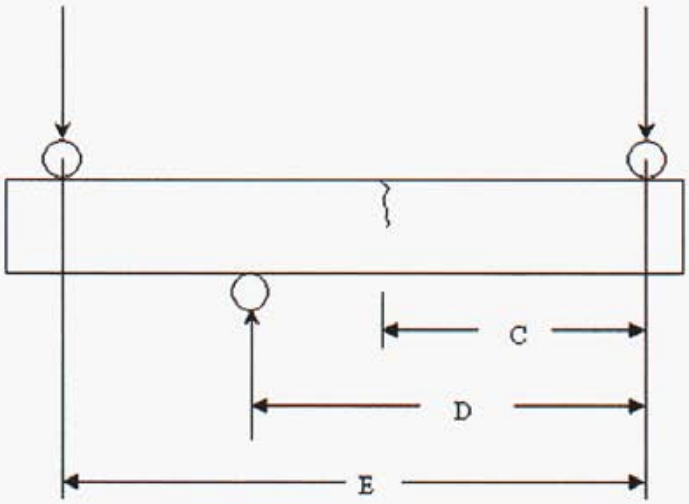

Sample	C, in	D, in	E, in
6061 -04	0.81	1.19	2.00
304-04	0.87	1.19	2.00

Figure 3.3: Mixed-mode loading was achieved by shifting the precrack and the reaction support away from center with respect to the load-line.

3.1.2 Results

Load versus displacement curves for two 6061 specimens are shown in Figure 3.4. Both curves show a rapid decrease in load following a maximum value, which is characteristic of crack propagation. Because the load-line was offset from the crack tip and because the mixed-mode fracture toughness is generally greater than mode I values, the maximum load was significantly greater for the mixed-mode test. Several unloadings were performed during the mode I experiment. Each unloading had a different slope, which also indicated crack growth. Images corresponding to the points labeled on the load curves are shown in Figure 3.5 and Figure 3.6. After removal from the SEM, the fracture surfaces were examined. The image shown in Figure 3.7 is typical of the

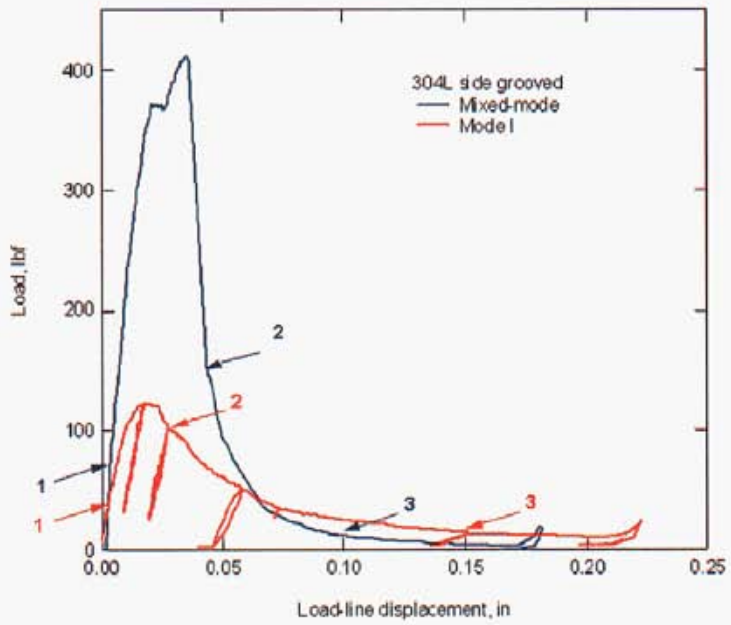

Figure 3.4: Load curves for specimens of 6061 aluminum recorded during straining in the SEM. The numbered points correspond to specimen images shown in Figures 3.5 and 3.6. Dropping load after a maximum is characteristic of crack propagation. The point labeled 2 on the mixed-mode curve is typical of a short crack advance referred to as pop-in. Several un-loadings were performed during the experiment.

fracture surfaces of 6061 specimens, which were characterized by mostly flat fracture with some shear-lip formation.

Load-displacement curves for two 304L specimens are shown in Figure 3.4. In contrast to the 6061 load data, the 304L curves show no drop in load, indicating that crack growth did not occur. The SEM images in Figure 3.9 and Figure 3.10 reveal extensive crack tip blunting with little evidence of crack propagation, in the fracture mechanics sense. Earlier SEM experiments with 304L specimens in the as-fatigue cracked condition revealed only crack tip blunting prior to reaching the displacement limit of the stage. As a result, both of the specimens shown here had been overloaded in the CT geometry prior to extracting the three-point bend geometry, which is why the cracks are blunted in Figure 3.9(a) and Figure 3.10(a). Examination of the SEM images and the specimens after the experiment suggested that the creation of new surface at the crack tip occurred through gross plasticity.

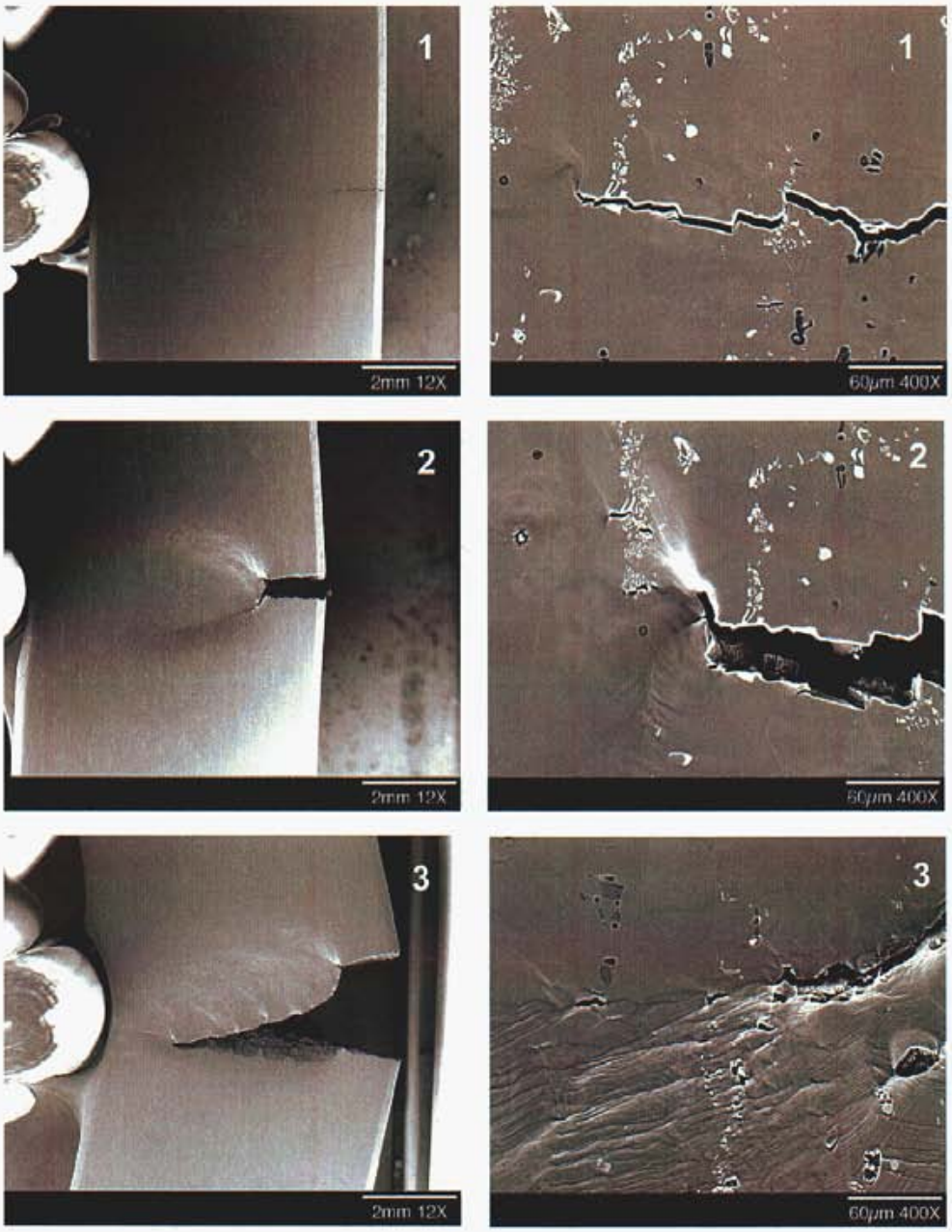

Figure 3.5: Images of a 6061 aluminum sample tested in mode I. In (2), the crack has advanced in the specimen interior, and the initiation of shear-lips has coincided with the formation of surface relief ahead of the crack tip. The 400× image labeled (3) shows shear bands and voids in the vicinity of the shear lips.

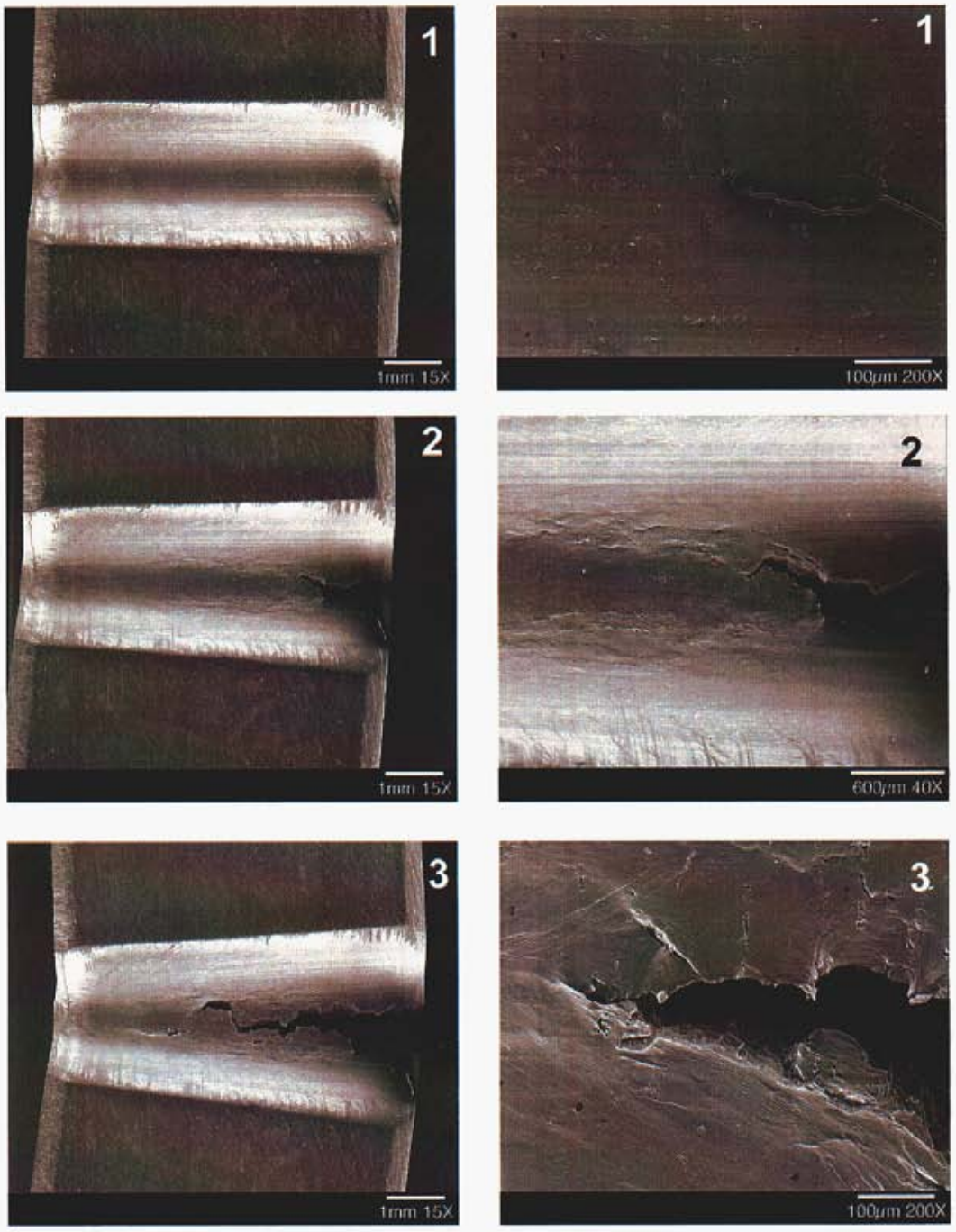

Figure 3.6: Images of a 6061 aluminum sample containing side grooves and tested in mixed-mode loading. The side grooves helped reduce the size of the shear-lips.

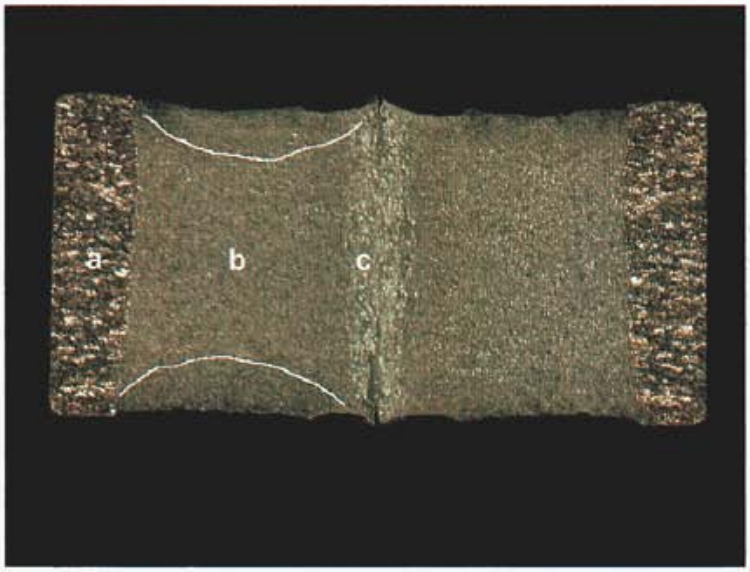

Figure 3.7: Image of the fracture surface on two halves (mirror images) of a 6061 aluminum sample tested in mode I loading. The load curve for this sample is shown in Figure 3.4. The fatigue precrack is visible in region (a), and the fracture surface extends through region (b). Region (c) is the remaining ligament at the end of the experiment. The extent of shear-lips is indicated by lines drawn over one-half of the sample.

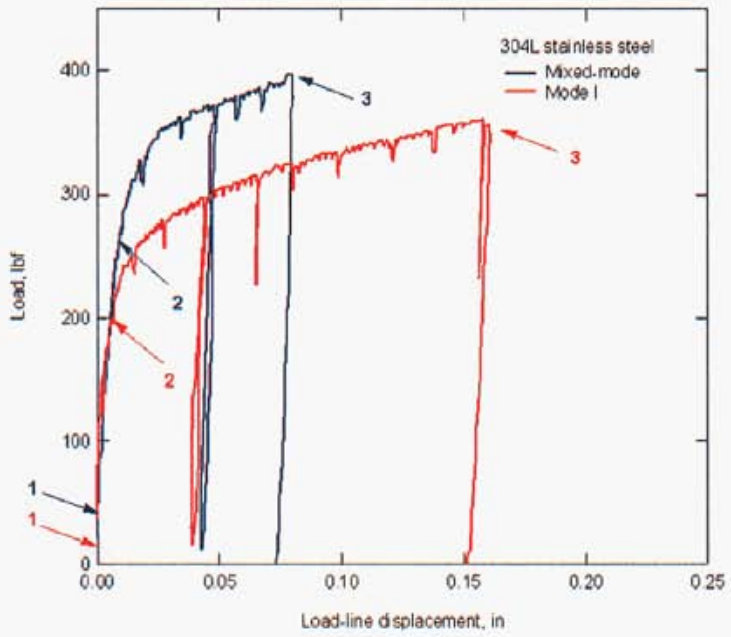

Figure 3.8: Load curves for specimens of 304L stainless steel recorded during straining in the SEM. Several un-loadings were performed during the experiments. Smaller drops in load resulted from stage relaxation while imaging the specimen. Smaller load serrations are artifacts from the manual gear drive of the stage. The load continued to increase with strain throughout the experiment, which indicated that the crack did not propagate.

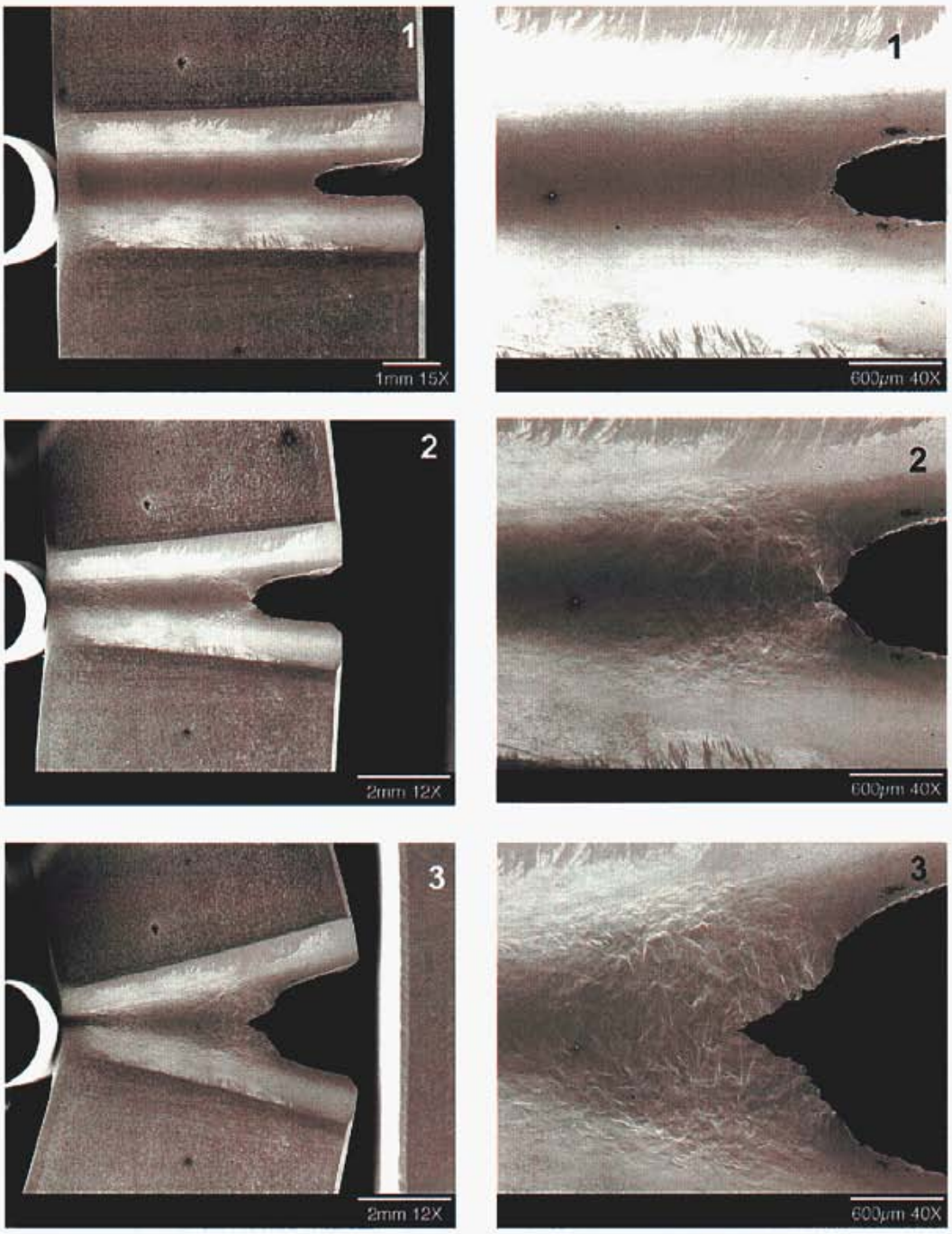

Figure 3.9: Images of 304L stainless steel sample loaded in mode I. The fatigue precrack in this sample had been blunted while in the CT geometry. The crack tip opening displacement continued to increase with strain. Creation of new surface at the crack tip occurred through gross plasticity.

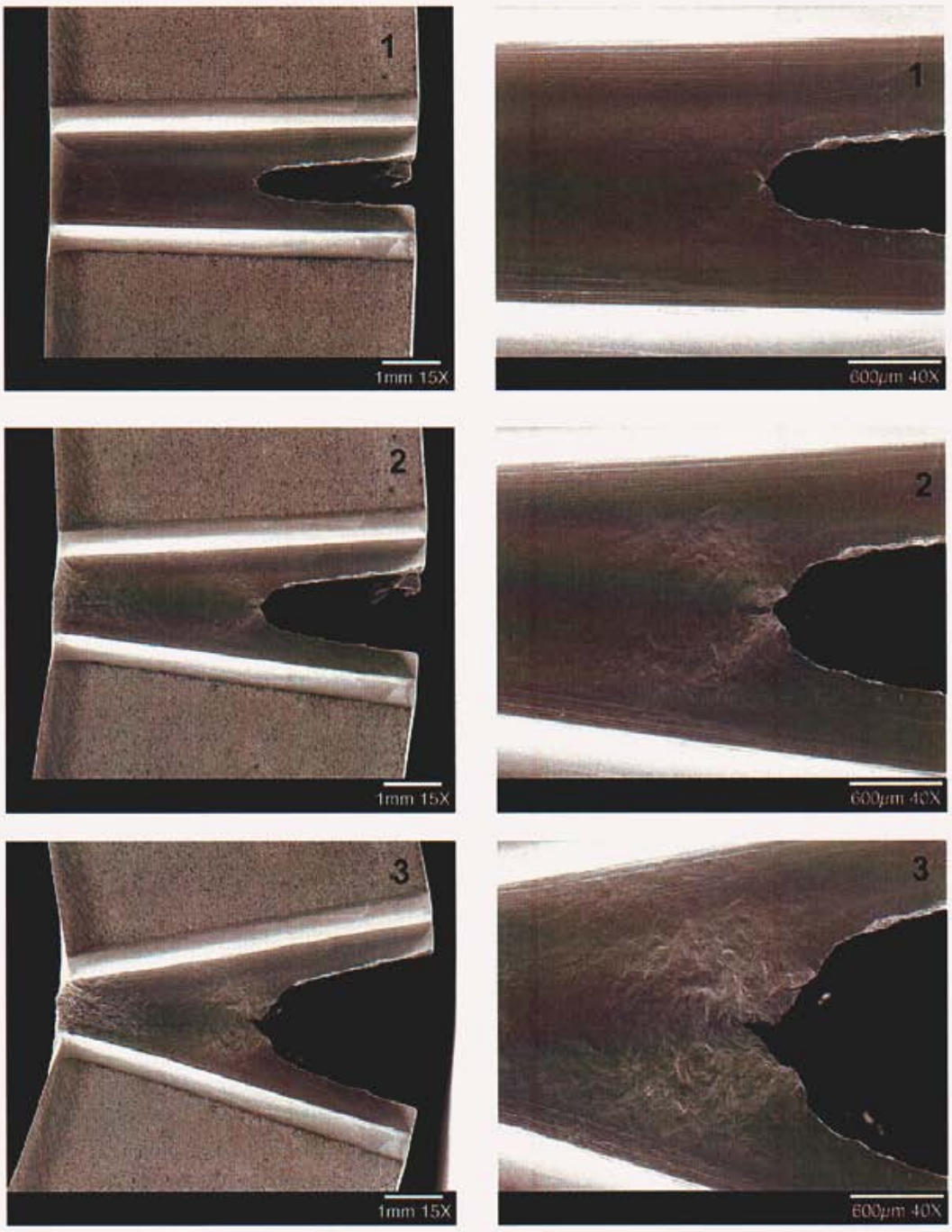

Figure 3.10: Images of 304L stainless steel sample under mixed-mode loading. The precrack in this specimen had been blunted while the sample was in the CT geometry. Throughout the experiment, the formation of crack-like features at the blunted crack tip was followed by additional blunting.

3.2 Plastic Zone Mapping

Measurement of the plastic zone developed during fracture is one measure of the fidelity of fracture modeling to fracture experiments. Various techniques for plastic zone mapping have been employed, and the results generally agree with estimates of plastic zone size obtained from elastic plastic fracture mechanics [26]. For this work, it was decided to pursue the development of a technique that would provide good spatial resolution, be applicable to a wide range of common alloys, allow post-test serial sectioning to reveal subsurface plasticity, and employ instruments readily available. Of the established techniques, microhardness measurements and the electron microscopy technique based on selected area channeling patterns (SACP) come closest to meeting all the criteria. However, microhardness measurements have limited spatial resolution, and SACP capability was not readily available. Another electron microscopy technique based on electron back-scatter diffraction (EBSD) patterns has been described in several publications [30, 28, 23, 29]. The method is based on image analysis techniques, which quantify the degradation in EBSD pattern quality that results from dislocation storage. The EBSD pattern quality technique has shown better spatial resolution than SACP (down to 200 nm), but more importantly, promised the potential to be implemented using any scanning electron microscope (SEM) fitted with a commercial EBSD system.

Electrons that back-scatter from a small volume of material below the surface of a crystalline solid are diffracted by the lattice. The resulting patterns contain light and dark bands, which correlate with diffracting planes and intersect at zone axes. Electrons are also scattered by dislocations and, and because dislocation structure appears random in comparison to the lattice, the sharpness of the EBSD pattern is reduced in proportion to the dislocation density. Wilkinson *et al.* [30, 28, 23, 29] showed that quantification of the pattern sharpness, or quality, can be obtained by looking at the higher-frequency fourier coefficients of the patterns. In their work, the EBSD patterns were captured on film because the digital cameras available on commercial systems at that time did not have the resolution and grayscale range to capture changes in pattern quality with sufficient sensitivity. Advances in EBSD system cameras and software presented the potential to record patterns directly and efficiently with resolution and grayscale range sufficient to capture pattern quality degradation due to dislocation storage.

3.2.1 EBSD Experimental Details

Quantification of strain using the EBSD pattern quality requires calibration based on specimens that have been strained to a known amount. Calibration specimens were prepared by performing interrupted tensile tests on 304L stainless steel and 6061 aluminum, obtained from the same lot as the three-point bend specimens. True stress/true strain curves for the samples are shown in Figure 3.11 and Figure 3.12. Using this approach, it is assumed that the effect on pattern quality of the dislocation structure developed in uni-axial tension is similar to the effect of the dislocation structure developed by the plain strain and plain stress conditions that make up the plastic zone developed during fracture. The tensile samples were sectioned, mounted with the tensile axis normal to the mount surface, ground, polished, and lightly etched. The importance of a clean surface

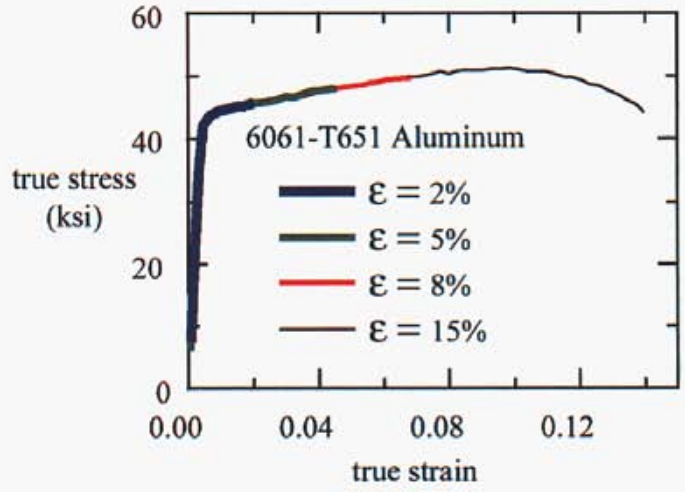

Figure 3.11: Tensile stress-strain curves for samples of 6061 aluminum used as calibration specimens for EBSD pattern analysis. The tests were interrupted at different levels of strain. Samples were sectioned, and prepared for EBSD pattern capture.

for EBSD work is recognized in general, and the effect on strain measurements was investigated for 6061 aluminum [28]. An electro-polish was tried on the 6061 aluminum, but SEM images and EBSD patterns showed that the light chemical etch provided better results. Strain was determined for each calibration specimen by measuring the diameter of the polished surface, and comparing it to the as-machined diameter of the tensile samples.

Specimens were imaged in a Jeol JSM-6700F field emission SEM fitted with an Qxford Instruments, Inca EBSD system. Locations for EBSD pattern capture were selected such that the patterns would likely not be influenced by grain boundaries or precipitates. Representative images of 304L and 6061 in the as-received condition are shown in Figure 3.13. For each set of patterns collected, a background intensity map was recorded by scanning the electron beam over an area. The background intensity arises from the sample, and the sample/detector geometry. Because the beam was scanned over an area, specific diffraction information was lost, resulting in a diffuse distribution of intensity that can be subtracted out from the EBSD patterns. The patterns were captured from point locations using an integration time of around 100 seconds, and recorded without binning in 1024 × 1013 pixel image files.

Analysis of the EBSD patterns was performed around a 110 zone axis. The location of the zone axis was identified on the patterns, and a 400 × 400 pixel area was cropped from the original pattern image. The same location was cropped from the background image, and the background intensity was subtracted from the pattern. Line scans were extracted from the pattern image along circular paths about the zone axis. The grayscale values for the line scan were determined from the average of ten pixels either side if the path. A discrete fourier transform (DFT) was performed on the line scan. Windowing was not used prior to the DFT because the closed circular paths provided a periodic waveform. Because changes in pattern quality are primarily due to bands becoming more

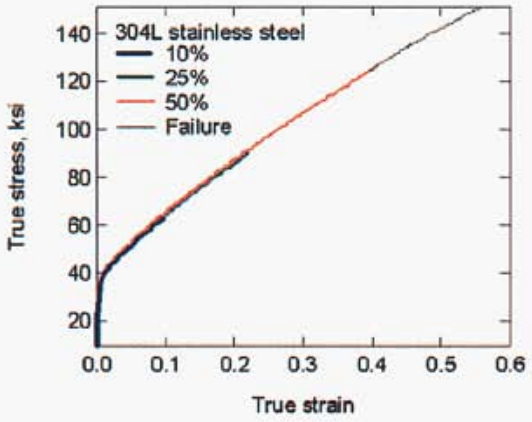

Figure 3.12: Tensile stress-strain curves for samples of 304L stainless steel used as calibration specimens for EBSD pattern analysis. The tests were interrupted at different levels of strain. Samples were sectioned, and prepared for EBSD pattern capture.

diffuse with strain, the circular paths allowed the one-dimensional DFT to be applied in a way that would be most sensitive to changes in the sharpness of the bands. A power spectrum density (PSD) was calculated from the square root of the sum of the squares of the real and imaginary fourier coefficients. A power spectrum first moment (PSFM) was calculated by multiplying the PSD values by their frequency, and summing the products. The pattern quality was represented by the single value PSFM for each circular path about the zone axis.

3.2.2 EBSD Results

Representative EBSD patterns for 304L and 6061 are shown in Figure 3.14 and Figure 3.15, respectively. The 304L patterns are sharper than the 6061 patterns because a higher yield of backscattered electrons is obtained from higher atomic number elements. The patterns show a qualitative decrease in sharpness with an increase in strain. However, the PSFM values for 304L and 6061 calibration samples are unable to distinguish between the as-received condition and the other calibration samples. These results are disappointing, and it is not clear why the method failed. One possibility is that the digital camera is not capable of capturing the necessary pattern detail, just as was the case for earlier generation imaging systems. The EBSD patterns are of very low intensity, and perhaps it is necessary to record the patterns on film and then use a dedicated film scanner to digitize the patterns. However, if we assume that the camera is capable of capturing the required detail, then other factors could be addressed. The integration time to record each pattern could be increased, although modifications to the Inca software may be required to do so. The electron back scatter yield could be increased by using an instrument with a tungsten filament rather than the field-emission microscope to which the Inca EBSD system was fitted.

Another issue to consider is the effect of the specimen surface. Others have shown [28] that

contamination from the electron beam of the SEM can severely degrade the pattern quality after viewing the surface at high magnification for even short periods of time. While we took precautions to have well-prepared surfaces, and the SEM operator was careful not to view the diffraction sites longer than necessary, it is still possible that surface conditions played a role. Additional efforts to understand the capabilities of EBSD pattern quality measurements using digital image capture could only be accomplished with direct access to electron microscopy facilities. For that reason, it was decided to discontinue our efforts to map plastic zones using EBSD pattern quality.

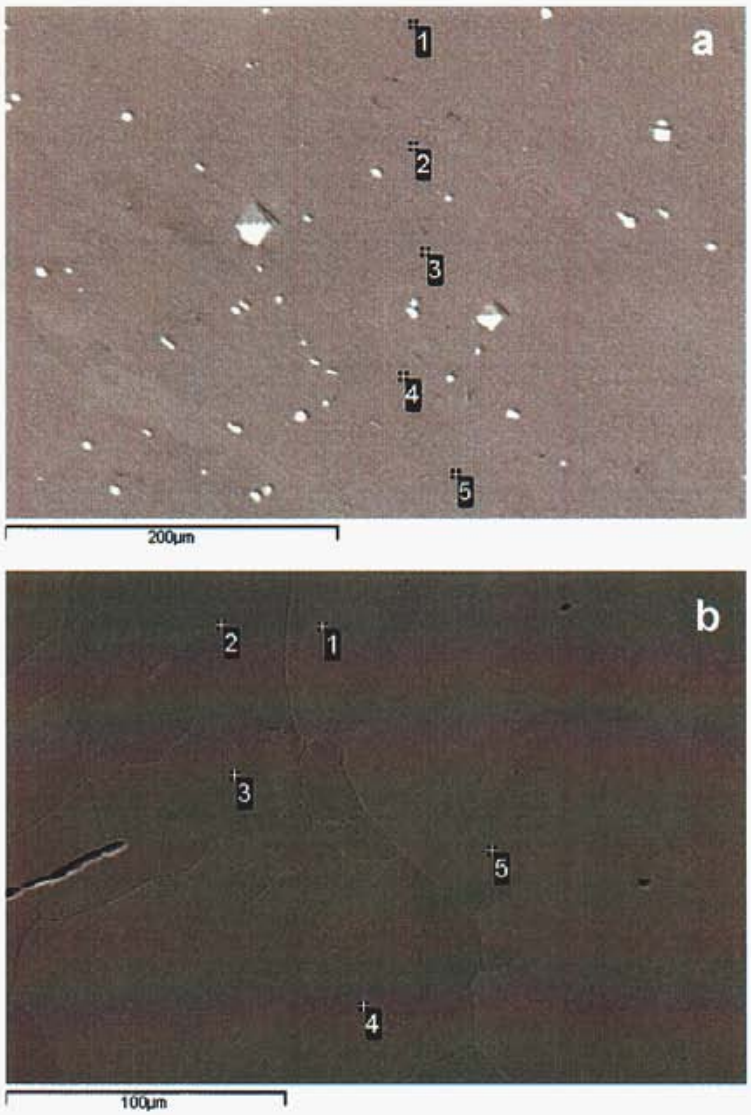

Figure 3.13: Secondary electron images of (a) 6061 aluminum and (b) 304L stainless steel in the as-received condition. Numbers on the images indicate points from which EBSD patterns were captured.

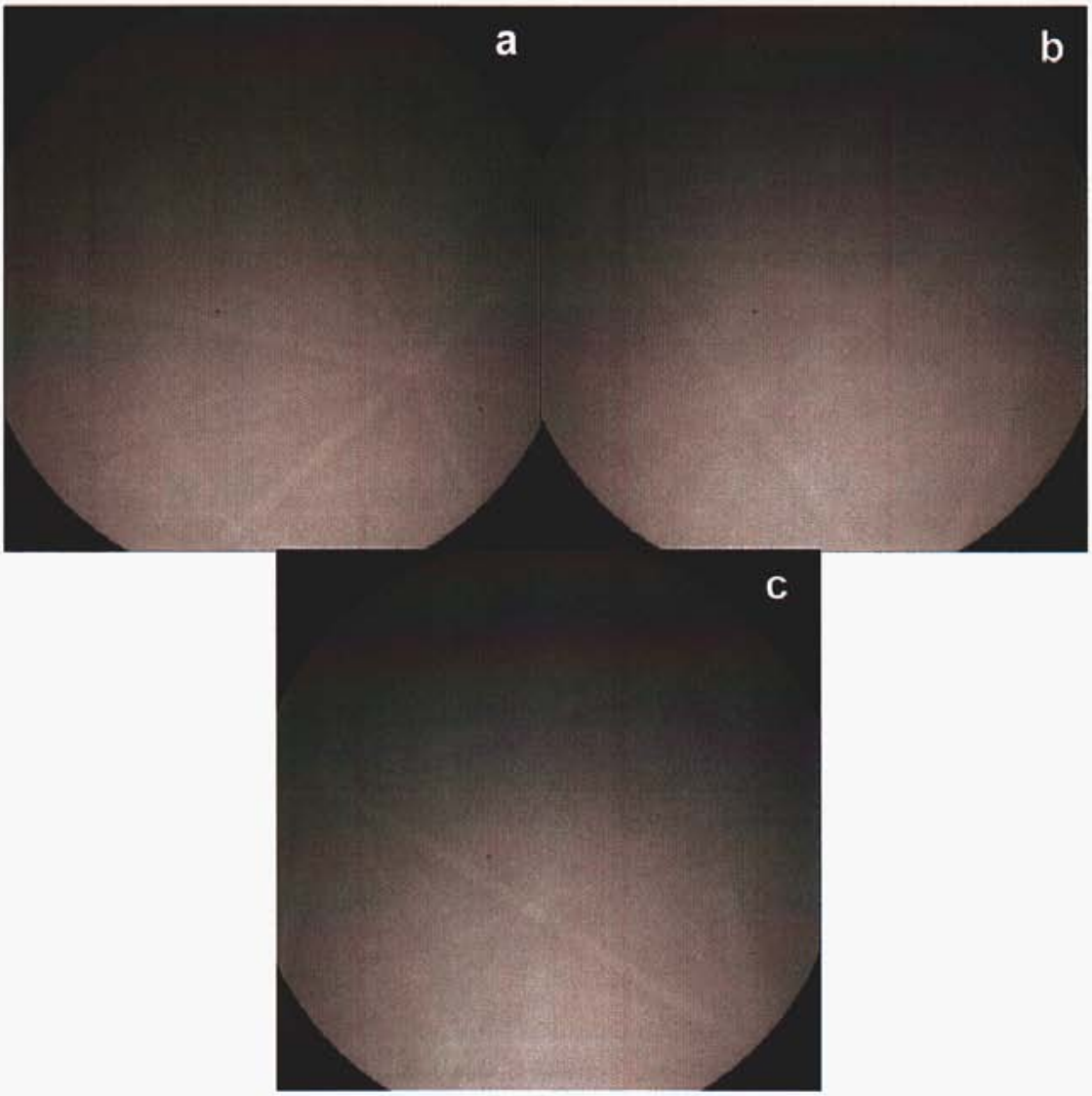

Figure 3.14: Representative EBSD patterns from 6061 aluminum: (a) as-received, (b) 2% strain, (c) 15% strain. A qualitative degradation in pattern quality with strain is apparent. However, even in the as-received condition the patterns were not very sharp.

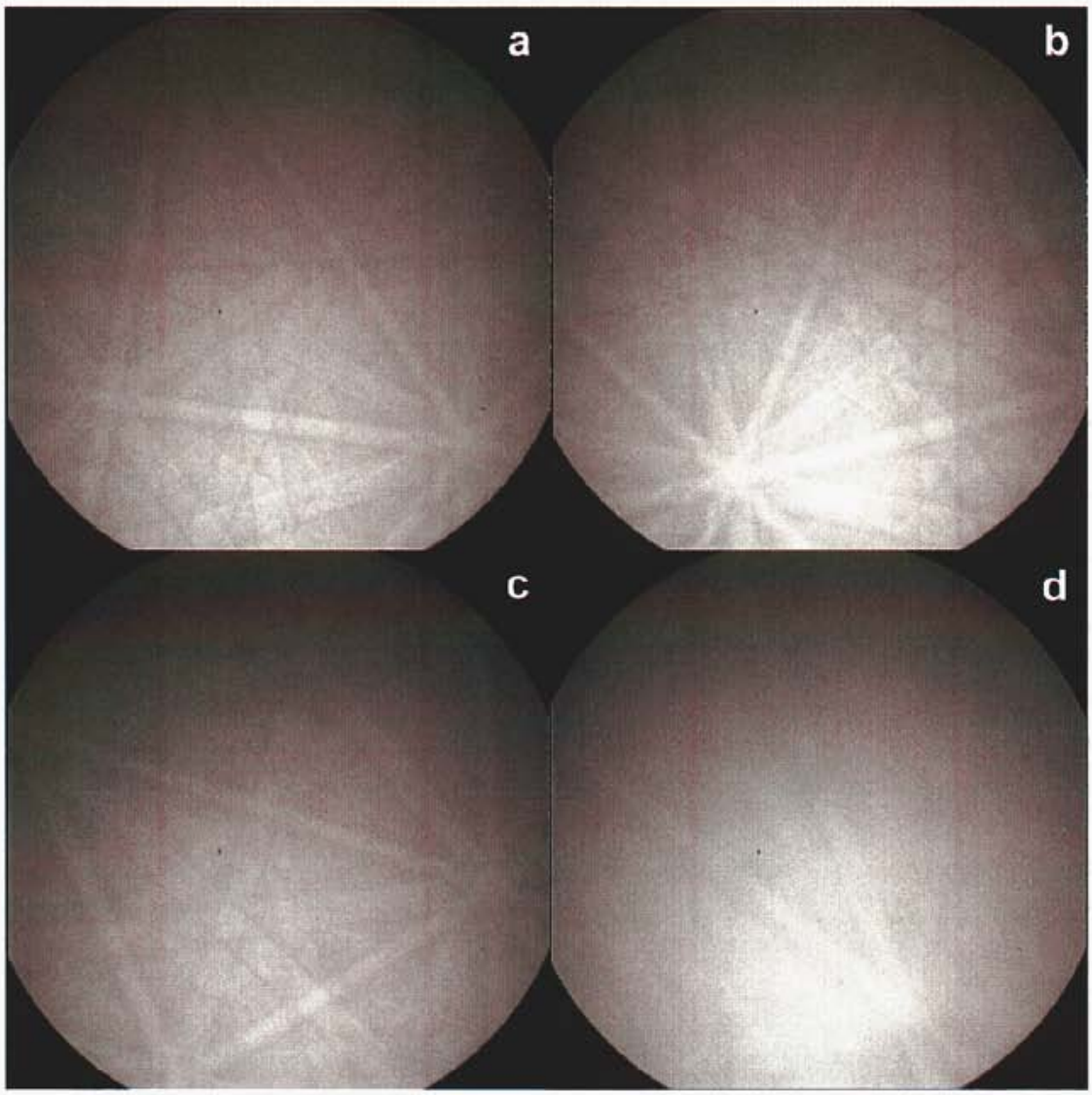

Figure 3.15: Representative EBSD patterns from 304L stainless steel: (a) as-received, (b) 10% strain, (c) 25% strain, (d) 50% strain. A qualitative degradation in pattern quality with strain is apparent.

This page intentionally left blank.

Chapter 4

Numerical simulations

In this chapter, we present numerical examples to demonstrate the response of the cohesive zone model described in Section 2.3.3 subject to quasistatic loading conditions undergoing two-dimensional, plane strain deformations. In the first example, we attempt to embed the nonlinear fracture process zone within a remote K-field. Under conditions of small-scale yielding, this approach allows us to determine the crack growth behavior for a specific, remotely applied crack driving force. In the second example, we attempt to model the three-point bending experiments described in Section 3.1. For both examples, the parameters for the bulk material response are selected to fit 6061-T6 aluminum, as listed in Table 2.1 at 297 K. The parameters for the cohesive model are the same as those used in the examples in Section 2.3.3 unless explicitly noted. The cut-off value for the damage in the zone is limited to $\phi_{\max} = 95\%$, above which the zone produces no tractions.

Because of nonlinearities resulting from the constitutive response and crack extension, the solutions in the examples must be determined by an iterative procedure. For the calculations performed in this study, we experienced the greatest stability and efficiency with a Newton's method solver. We seek to determine the degrees of freedom $\mathbf{u}$ to satisfy force equilibrium,

$$\mathbf{N}(\mathbf{u}) = \mathbf{F}^{\text{ext}}(t), \tag{4.1}$$

where the internal force $\mathbf{N}(\mathbf{u})$ is a nonlinear function of the displacements and the external force $\mathbf{F}^{\text{ext}}$ due to the boundary conditions has prescribed values in time. For these quasistatic calculations, time may be interpreted as a "progress" variable. At the i^{th} iteration of the solution procedure for which equilibrium is not satisfied, the residual force $\mathbf{R}$ is given by

$$\mathbf{R}^{(i)} = \mathbf{F}^{ext}(t) - \mathbf{N}(\mathbf{u}^{(i)}). \tag{4.2}$$

At iteration $i + 1$, we seek $\mathbf{R}^{(i+1)} = \mathbf{0}$. Expressing $\mathbf{R}^{(i+1)}$ with a first order Taylor expansion of (4.1) at $\mathbf{u}^{(i)}$ yields

$$\mathbf{R}^{(i+1)} = \mathbf{R}^{(i)} - \mathbf{K}^{(i)}\,\Delta\mathbf{u}^{(i)}, \tag{4.3}$$

where $\mathbf{K}$ is the tangent stiffness derived from $\mathbf{K} = \frac{\partial \mathbf{N}}{\partial \mathbf{u}}$. For optimal convergence of the solution procedure, we use the consistent linearization of the internal force, which includes the linearization

of the cohesive response given in 2.30. From (4.3), the displacement update is given by the solution of the linear system

$$\Delta \mathbf{u}^{(i)} = \left[\mathbf{K}^{(i)}\right]^{-1} \mathbf{R}^{(i)}, \tag{4.4}$$

from which we calculate the next iterate of the displacements as

$$\mathbf{u}^{(i+1)} = \mathbf{u}^{(i)} + \Delta \mathbf{u}^{(i)}. \tag{4.5}$$

Th process of forming and solving (4.4) is repeated until the magnitude of the residual force is below a chosen tolerance. The tolerance used for the calculations in this study was $\|\mathbf{R}^{(i)}\|/\|\mathbf{R}^{(0)}\| < 10^{-8}$, where $\|\mathbf{R}^{(0)}\|$ is the initial magnitude of the residual force after the boundary conditions have been incremented.

Because the bulk constitutive model uses a volume preserving formulation of plastic deformation, all of the calculations employ 4-noded, mixed elements with piecewise constant pressures (Q1P0) [20] to avoid problems with volumetric locking. Although the crack tip deformations are expected to be large, an element formulation limited to linear (infinitesimal) kinematics of deformation is used because of instabilities that were encountered due to strain localization in the bulk. The abundance of strain energy in the material surrounding the crack tip causes the onset of strain localization due to damage evolution to be very abrupt. These difficulties are exacerbated by geometric effects with finite strain formulations. Methods for stabilizing the damage evolution surrounding the crack tip are a topic of ongoing study. All calculations were performed with Tahoe *.

4.1 K-field simulations

In Section 2.3.2 and 2.3.3, we presented the response of the cohesive zone models under isolated conditions, free of interactions with surrounding material. These results are analogous to material point calculations for evaluating the response of bulk constitutive models. Although the calculations are helpful for establishing the effect of the various model parameters, they are insufficient to reveal the crack growth behavior that the models would predicted in simulations of realistic geometries. In those cases, there is the tight coupling between the cohesive zone and bulk constitutive response. As a result, determining parameters for the cohesive models requires solution of complete boundary value problems.

The experimental results described in Section 3.1 provide macroscopic load versus displacement information that is required for determining the model parameters. However, global information like this is not ideal for selecting parameters which determine the detailed response of the material in the fracture process zone. Ideally, we would like highly detailed information about the deformation fields around the crack tip. The *in situ* SEM observations did provide some guidance regarding the characteristic length scales of the fracture process zone. In particular, the micrographs reveal the scale of the model parameter w_0, the width of the fracture process zone (thickness perpendicular to the crack growth direction). They also reveal the length of the fracture process

*http://tahoe.ca.sandia.gov

zone (size along the crack growth direction) which is not a model parameter, but depends strongly on how quickly tractions decay with opening displacement. At the scale of the entire nonlinear region encompassing the crack tip, the experiments also reveal the crack opening angle which is indicative of the amount of plastic deformation accompanying crack extension.

One of the difficulties with fracture in inelastic materials is determining the crack driving force and subsequently the work to fracture. Cohesive approaches to modeling fracture address this issue by prescribing models for the dissipation of fracture directly. As a result, crack extension occurs, without requiring evaluation of the crack driving force or fracture criteria, once the work supplied to the fracture process zone reaches the dissipative capacity of the cohesive model. However, selection of parameters for the cohesive models still requires solution of some boundary value problems for which the crack driving force is well-defined. For this purpose, one could employ steady state crack growth conditions, such as those provided by an infinite strip. To determine the crack growth behavior predicted by the yield-point cohesive model described in Section 2.3.3, we embed the entire nonlinear fracture process zone within a K-field applied at the boundaries.

4.1.1 Simulation procedures

The scale of the plastic zone surrounding a crack tip can be estimated by [25]

$$r_p = \frac{1}{3\pi}\left(\frac{K}{\sigma_y}\right)^2. \tag{4.6}$$

Using an initial yield stress of 275 MPa for 6061-T6 given by the model parameters in Table 2.1 at 297 K and a fracture toughness of 29 MPa$\sqrt{\text{m}}$, we find $r_p \approx 1.2$ mm. Guided by this length scale, we construct the model geometry shown in Figure 4.1. The disc has a radius of 25 mm, while a 1×1 mm region near the crack tip is meshed with a regular grid of square elements. To verify the solutions are independent of mesh size, two meshes are constructed with $h = \{0.005, 0.0145\}$ mm in the near tip region. A pre-existing crack extends from near the center of the disc outward to the left edge.

In order to get a well-defined crack driving force, we assume that at a sufficiently large distance from the crack tip, the displacements follow Irwin's[11] isotropic, linear elastic K-field solution

$$\mathbf{d}(\mathbf{X}, \mathbf{X}^*) = \frac{K_{\text{I}}}{2\mu}\sqrt{\frac{r}{2\pi}}\, \boldsymbol{f}_{\text{I}}(\theta, \nu) + \frac{K_{\text{II}}}{2\mu}\sqrt{\frac{r}{2\pi}}\, \boldsymbol{f}_{\text{II}}(\theta, \nu)\,. \tag{4.7}$$

In the expression for the displacements, $\{r, \theta\}$ are the polar coordinates of a point $\mathbf{X}$ with respect to a local coordinate origin $\mathbf{X}^*$ centered at the crack tip. The elastic properties of 6061-T6, namely the shear modulus μ and Poisson's ratio ν, are used to calculate the displacement boundary conditions. Following the small-scale yielding approximation, we assume the asymptotic displacement field is not significantly affected by the nonlinearities in the fracture process zone when the distance to the outer boundary is sufficiently large.

The solution procedure determines the nodal displacements that satisfy static equilibrium for successive increments of the prescribed boundary displacements (4.7). The stress intensity factors

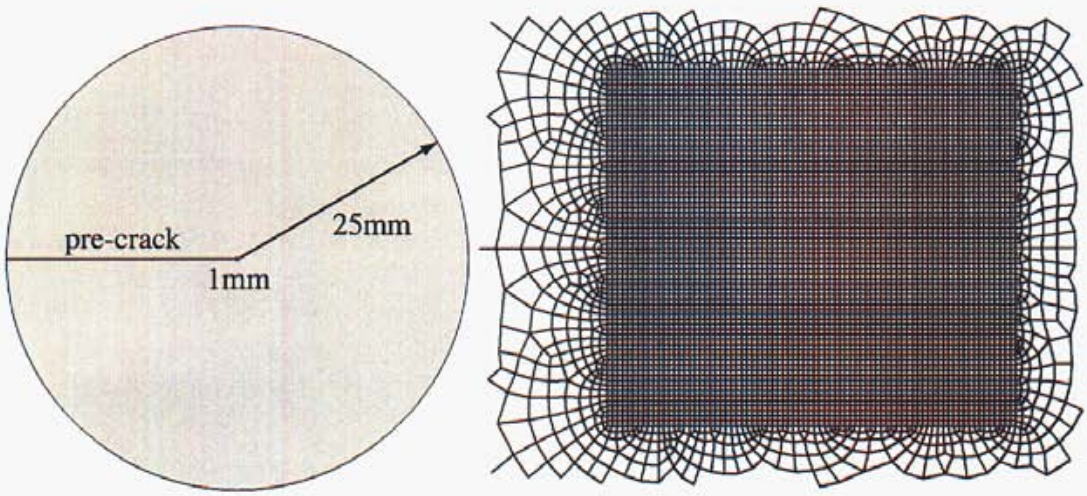

Figure 4.1: The geometry used for the K-field simulations and the near tip mesh with h = 0.0145mm.

$\{K_I, K_{II}\} = \{K_I(t), 0\}$ are increased monotonically until motion of the crack tip is detected. The crack tip is constrained to remain at the interface ($Y_0 = 0$) and is defined to be located along the crack extension direction at the farthest point at which the damage parameter exceeds the initiation damage for the cohesive model ($\phi > \phi_{\text{init}}$). Damage is used to track the crack tip rather than the location of the peak opening stress [13] because the crack tip plasticity causes the peak traction to occur on the cleavage plane at some distance ahead of geometric crack tip, where the material begins to separate to form the new crack faces.

If motion of the tip is detected, the displacement boundary conditions are adjusted for the new crack tip position and equilibrium is re-established. The stress intensity factors are incremented only if the tip remains stationary for the current values. Although the motion of the tip is often small compared with radius of the disc, the boundary conditions must be adjusted for the moving tip in order to simulate the approach to a steady-state fracture toughness value. With the moving tip procedure, the interface begins to "unzip" without additional increases in the stress intensity factors as the steady-state value is approached.

4.1.2 Results

Figure 4.2 shows the R-curve behavior produced by activating the zone for $\phi_{\text{init}} = \{0.5, 1, 2, 3, 4\}$ %. The calculation with $\phi_{\text{init}} = 5\%$ failed due to instabilities in the calculation. The curves indicate that the total dissipation increases as activation of the zone is delayed by selecting larger values of ϕ_{init}. The dissipation in the zone decreases as ϕ_{init} increases, indicating the bulk dissipation comprises the dominant portion of the total dissipation for the system. Notably, the R-curves do not reach a horizontal tangent, indicating that the cracks have not reached steady state. Since the mode I fracture toughness of 6061-T6 is approximately 29MPa$\sqrt{\text{m}}$, it is clear the calculations are

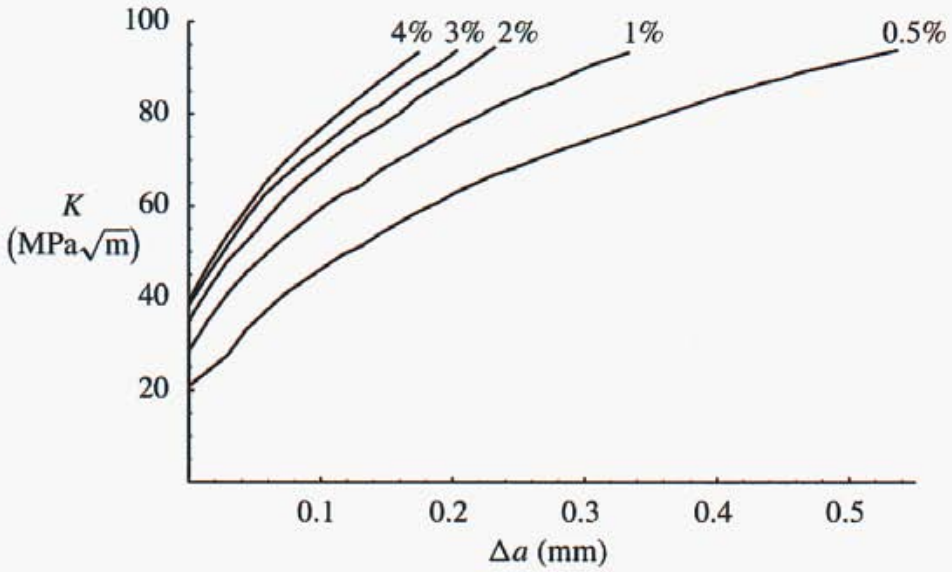

Figure 4.2: Comparison of the R-curve behavior for $\phi_{\text{init}} = \{0.5, 1, 2, 3, 4\}$ %.

overpredicting the work to fracture for the system. Over the range of ϕ_{init} plotted in the figure, there is relatively little change in the flow stress. This observation implies that the additional dissipation occurs not because the bulk stresses are higher, but because the crack tip is forced to "dwell" at a given position while the bulk damage mechanisms evolve.

Figure 4.3 shows a mesh refinement study for $\phi_{\text{init}} = 0.5\%$. Both meshes use a 1×1 mm uniformly meshed region near the tip, as shown in figure 4.1. However, the mesh size of the finer mesh is approximately three times finer than the elements used for the calculations shown in Figure 4.2. The results in the figure show that aside from differences for very small Δa, the curves agree very well, indicating that the dissipation becomes well-defined by introduction of the zone and that the simulation is independent of mesh size. Convergence in the solution of fracture simulations with cohesive methods requires that the mesh is sufficiently refined to capture the variation in traction in the fracture process zone. When combining bulk inelastic behavior with cohesive methods, the resolution requirements for capturing the solution in the bulk may be more or less restrictive than the mesh size required by the scale of the fracture process zone. The results in Figure 4.3 indicate the solution over the both bulk and cohesive surfaces are well-resolved. In addition, the imposed cut-off in the cohesive zone response for $\phi > \phi_{\max}$ is not producing any difficulties with arriving at a converged solution.

The corresponding traction distribution along the cleavage plane is shown in Figure 4.4. As expected, the cohesive approach removes the stress singularity at the crack tip, although the tractions do still vary rapidly over the length marked l_{zone} where the cohesive relations are active. The figure indicates the length of the fracture process zone is approximately $l_{\text{zone}} \approx 300\mu$m. Some features resulting from the discretization of the cleavage plane are evident in the distribution although they apparently do not produce any significant artifacts in the predicted R-curve. Looking closely at

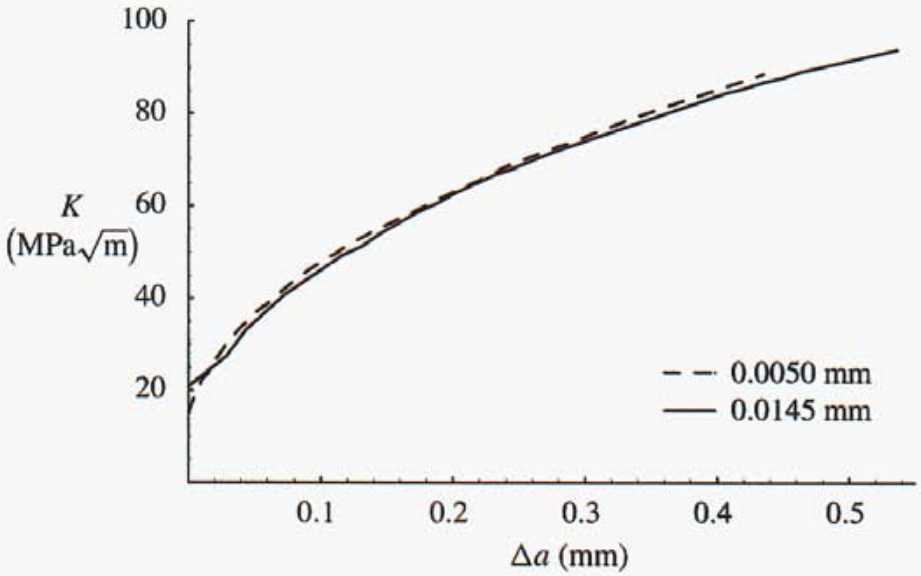

Figure 4.3: Comparison of the R-curve behavior with $\phi_{\text{init}} = 0.5\%$ for $h = \{0.005, 0.0145\}$ mm showing the results are nearly independent of the mesh size.

the micrographs in Figure 3.5 of the latter stages of growth in the 6061-T6 specimen, we see that this length appears larger than the approximately 150μm size of the process zone shown in the figure. Of course, the micrographs only provide information about the crack front at the surface; however, the overestimation of the fracture process zone by the calculations is consistent with the overestimation of the work to fracture demonstrated in Figure 4.2.

We can gain additional insight into the fracture process by plotting the opening rate as a function of opening for several positions along the cleavage plane. These results are presented in Figure 4.5. The curve (a) corresponds with the history of the opening rate at the initial crack tip position, curve (d) corresponds with the history for a point 0.38 mm ahead of the initial crack tip, while curves (b) and (c) show the history at intermediate positions. The opening rate is computed from the opening displacement results through a finite difference calculation. This operation tends to produce quite "noisy" results, so smoothing is applied to generate the curves shown in the figure. The unsmoothed results are shown for curve (a). There are several trends evident in the results. Points like (a) and (b) on the fracture surface close to the initial crack tip position experience a more gradual transition to the long-time opening rate than points which undergo fracture later, under conditions closer to the final steady-state such as points (c) and (d). This final long time rate increases with position along the fracture path, although all the opening rates for these calculations remain below levels at which rate-dependence in the zone is expected to become significant (see Figure 2.75).

The difference in hardness along the fracture path due to the statistically-stored dislocations represented by κ is shown in Figure 4.6. The values of κ do exhibit fluctuations in the values which are "frozen" into the cohesive relations behind the moving crack tip. These fluctuations are

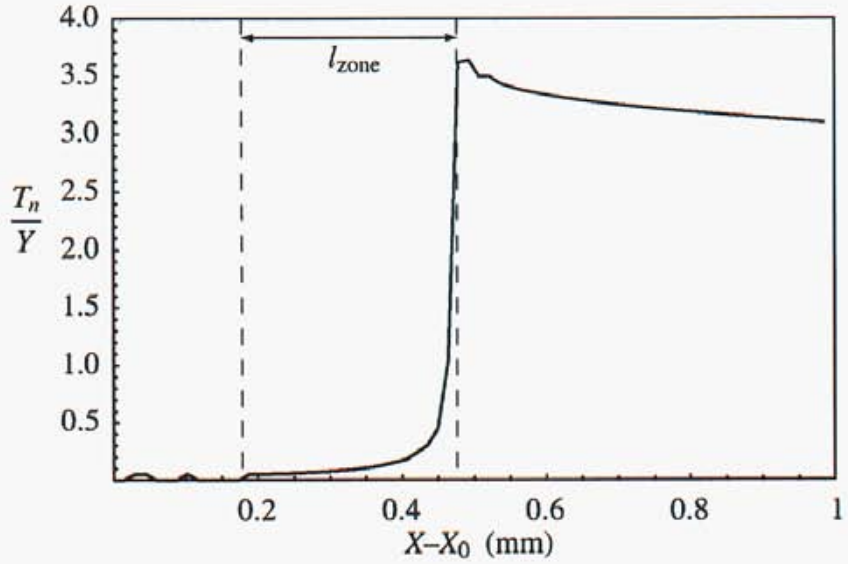

Figure 4.4: Distribution of the normal tractions T_n along the cleavage plane for $\phi_{\text{init}} = 0.5\%$ showing a cohesive zone size $l_{\text{zone}} \approx 300\mu$m.

an artifact of the numerical solution procedure. There is a distinct decrease in the hardness due to κ along the surface of the material as the crack propagates away from its initial position. This change indicates more plastic strain is occurring in the material during the transient state of growth than later as the growth approaches a steady-state. We would expect this behavior since the initial crack position furnishes less constraint for the material surrounding the tip. The results shown in the figure highlight how the properties, namely the yield stress, in the cohesive can vary with position depending on propagation conditions. In this case, the effect is not significant ($< 5\%Y$), but would be more pronounced with materials that display strong isotropic hardening.

The sequence of images in Figure 4.7 shows the evolution of plasticity surrounding the moving crack tip as the growth conditions approach steady-state. The 1×1 mm regular mesh near the crack tip is shown with filled contours, while the mesh is shown in outline for the surrounding region. The images show that the moving crack is leaving behind a plastic wake, which contributes to the increasing fracture resistance. The shape of the crack opening profile exhibits almost flat surfaces rather than the cusp-like profile associated with cohesive crack tips in elastic materials. A full-field view of the plastic zone around the crack tip is presented in Figure 4.8(a), showing it probably exceeds the scale at which we can assume small-scale yielding from the perspective of the disc boundary. The distribution of damage around the crack tip is shown in Figure 4.8(b). The results show that the damage is heavily concentrated along the surfaces of the crack, driven by the large hydrostatic stresses ahead of the crack tip. The damage in the first layer of elements along the crack face does display nonsmoothness, which quickly disappears with distance from the crack surface.

In conclusion, the results presented in this section indicate that the total work to fracture is

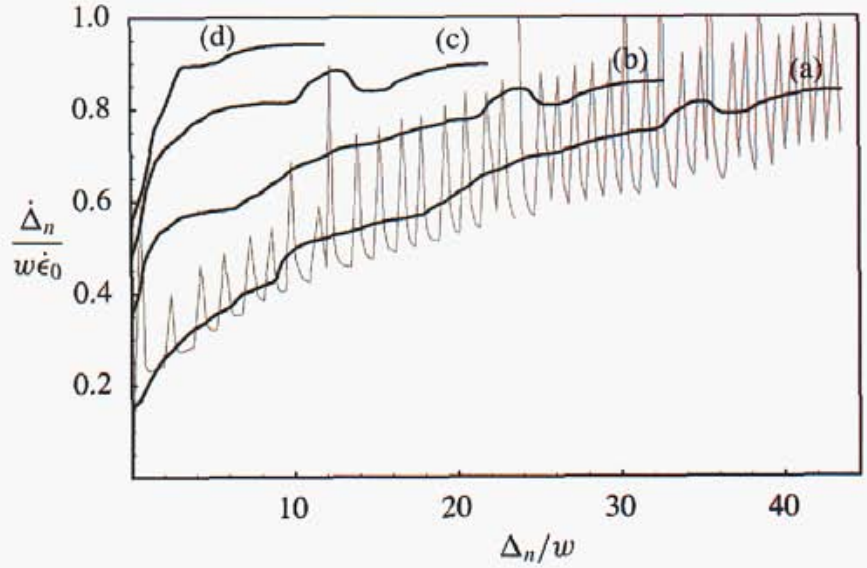

Figure 4.5: The smoothed opening rate as a function of opening at positions $X - X_0 =$ (a) 0.0, (b) 0.12, (c) 0.25, and (d) 0.38 mm ahead of the original crack tip position X_0 for $\phi_{\text{init}} = 0.5\%$. The raw, unsmoothed values are shown for (a).

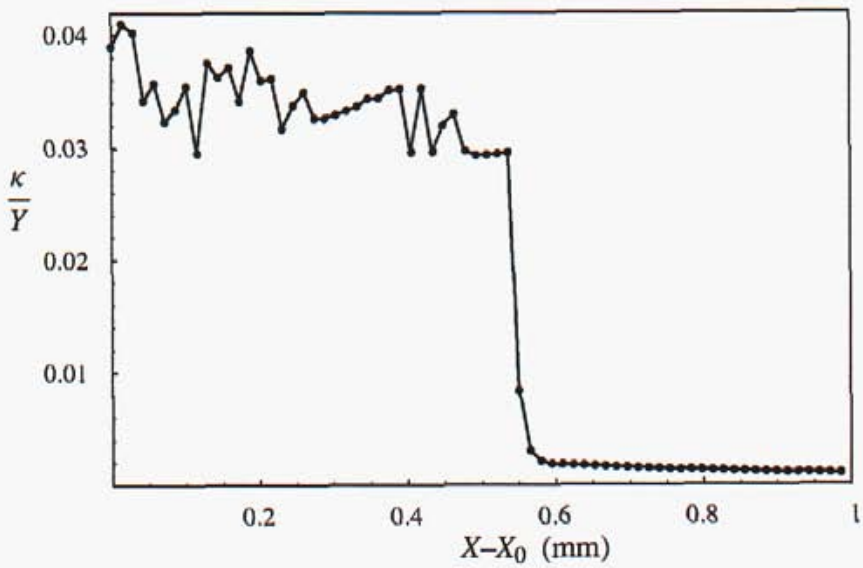

Figure 4.6: The distribution of the hardening state variable κ along the cleavage plane. κ ahead of the current crack tip position $(X - X_0) \gtrsim 0.5$ is still evolving as dictated by the surrounding bulk material, while κ behind the crack tip $(X - X_0) \lesssim 0.5$ is frozen since we prescribe $\dot{\kappa} = 0$ in the cohesive model.

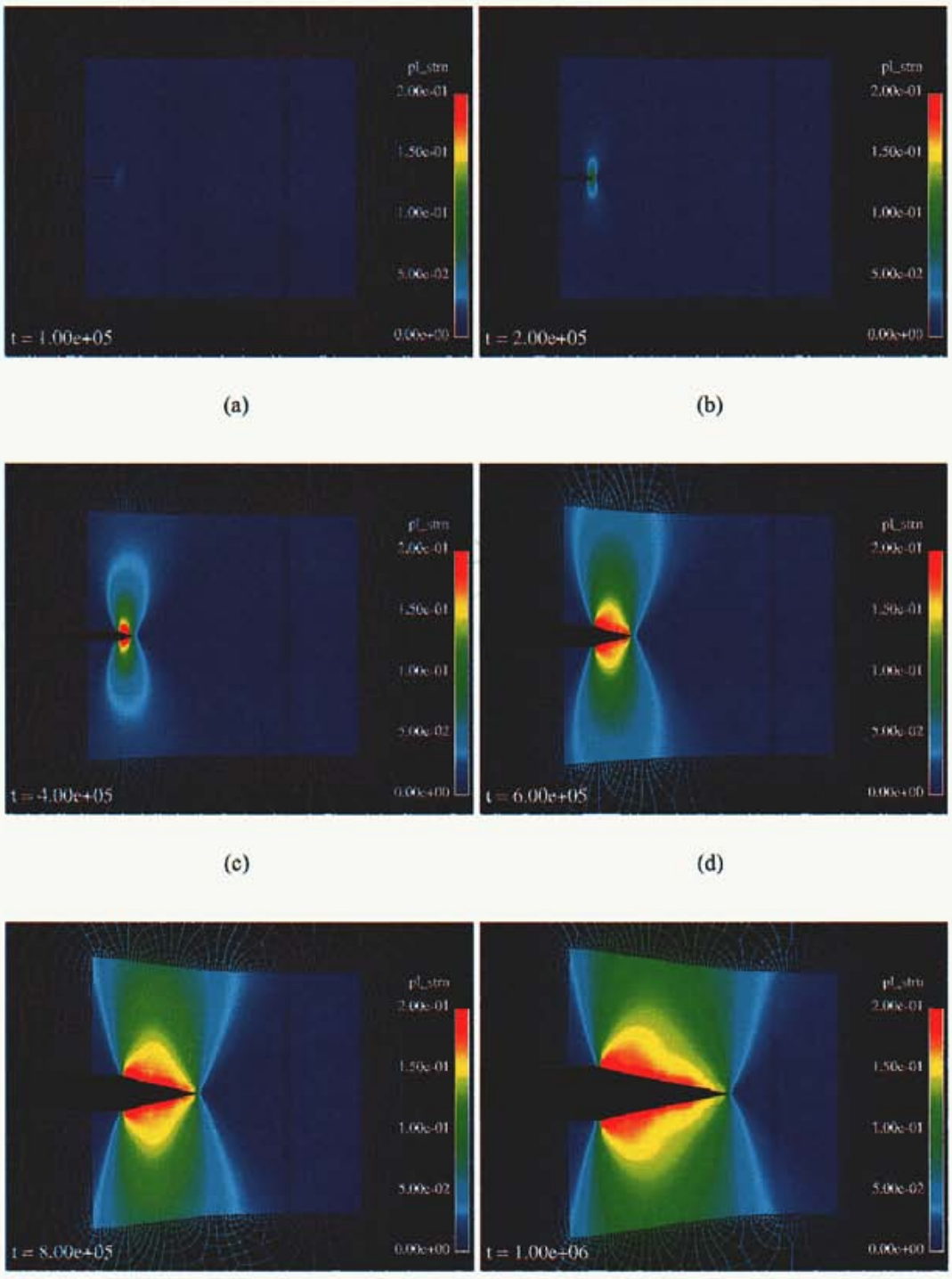

Figure 4.7: A sequence of images showing contours of the equivalent plastic strain for the case $\phi_{\text{init}} = 0.5\%$. The time t shown is expressed in 10^{-4} seconds.

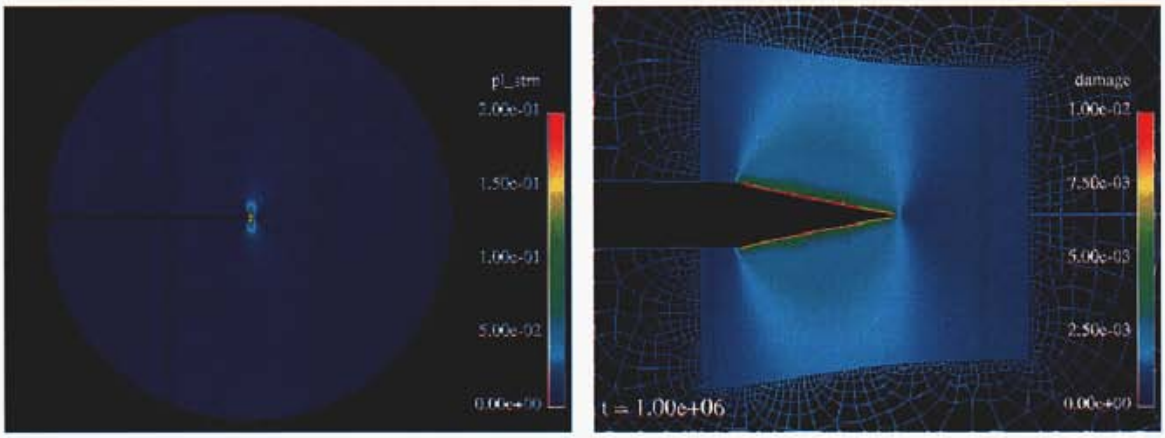

(a) (b)

Figure 4.8: Results of the calculations with applied K-field boundary conditions for $\phi_{\text{init}} = 0.5\%$ showing (a) contours of the equivalent plastic strain plotted over the whole disc geometry and (b) contours of the damage ϕ plotted over the 1×1 mm near tip region.

overpredicted by the parameters selected for the cohesive relations. We suspect the calculations are overpredicting the amount of plastic dissipation in the bulk surrounding the crack tip. Detailed experimental measurements of the plasticity surrounding the crack tip would be very helpful for improving the model predictions. The results indicate that the work to fracture predicted by the simulations could be reduced by choosing smaller values of ϕ_{init}, which already has surprisingly low values. Defects may be playing a key role in producing the discrepancy between the simulation results and the experimental observations. ϕ is a measure of distributed damage, while the *in situ* observations clearly show the crack path meandering between sources of stress concentration, such as second phase particles, grain boundaries, and persistent slip bands. Inhomogeneities like these may dominate the process of strain localization ahead of the crack tip. In any case, further parametric studies need to be performed to determine the parameters needed to produce more reasonable predictions of the fracture energy.

The results indicate that the total dissipation increases as ϕ_{init} increases, despite the fact the zone's contribution to the total dissipation decreases under these conditions. This behavior clearly demonstrates the complicated interaction between the bulk and cohesive models with these materials. The dramatic increase in the total dissipation is not simply a result of higher tractions in the fracture process zone, which don't vary much as $\phi_{\text{init}} \rightarrow 0$ but are instead due to the direct requirement of additional inelastic deformation of the bulk in order to reach the point at which the localized mode is activated. This is different from the dependence on the total dissipation on the cohesive stress shown by Tvergaard and Hutchinson [24] in which higher cohesive stresses triggered more extensive plastic deformation in the bulk. In our simulations, the interaction is the result of a direct connection between mechanisms of deformation within the bulk and fracture

process zone and not just coupling of mechanics.

4.2 3-point bending calculations

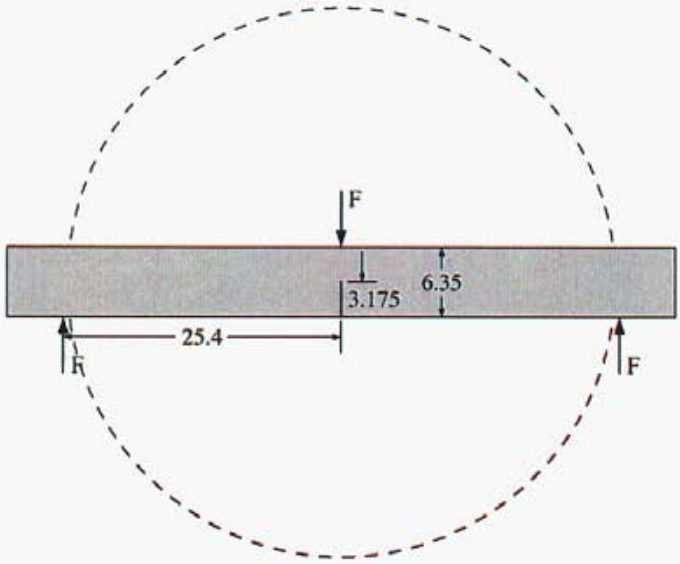

Figure 4.9: The geometry used for the three-point bending simulations. Dimensions are shown in millimeters. The size of the disc used for the K-field simulations is shown by the dashed circle.

In this section, we model the three-point bending experiments described in Section 3.1. The geometry and dimensions of the beam are shown in Figure 4.9, and are selected to match the dimensions of the experimental specimens. The beam has a height of 0.25 inches and a span of 2 inches. The initial crack length is $\frac{a}{w} = \frac{1}{2}$. The beam is shown together with a dashed circle indicating the scale of the disc used for the K-field calculations in Section 4.1. Clearly, the dimensions of the beam violate an assumption of small-scale yielding at the crack tip, therefore, we cannot determine the crack driving force from K or J. Under these circumstances, we must rely on the fact the dissipation *mechanisms*, not *amount*, remain the same for the small bending geometry as they are for the more idealized K-field simulations we use to characterize the model. This is underlying assumption behind cohesive approaches which focus on developing models for dissipation under general conditions rather than attempting to develop failure criterion which tend to be limited to specific growth conditions.

4.2.1 Simulation procedures

Parameters for the bulk and cohesive models are selected to represent 6061-T6, as described for the K-field calculations in Section 4.1. We select $w_0 = 5\mu$m and $\phi_{\max} = 95\%$. The value of

ϕ_{init} is varied to see its effect on the simulation results. We apply loads to the beam by prescribing displacement of the center pin with respect to the two pins supporting the span. The loading rates are selected to exercise the models in their rate-independent limits. The mesh size in the near tip region is $h \approx 0.015$ mm to capture the distribution of tractions in the cohesive zone and the details of the plastic zone in the surrounding material.

4.2.2 Results

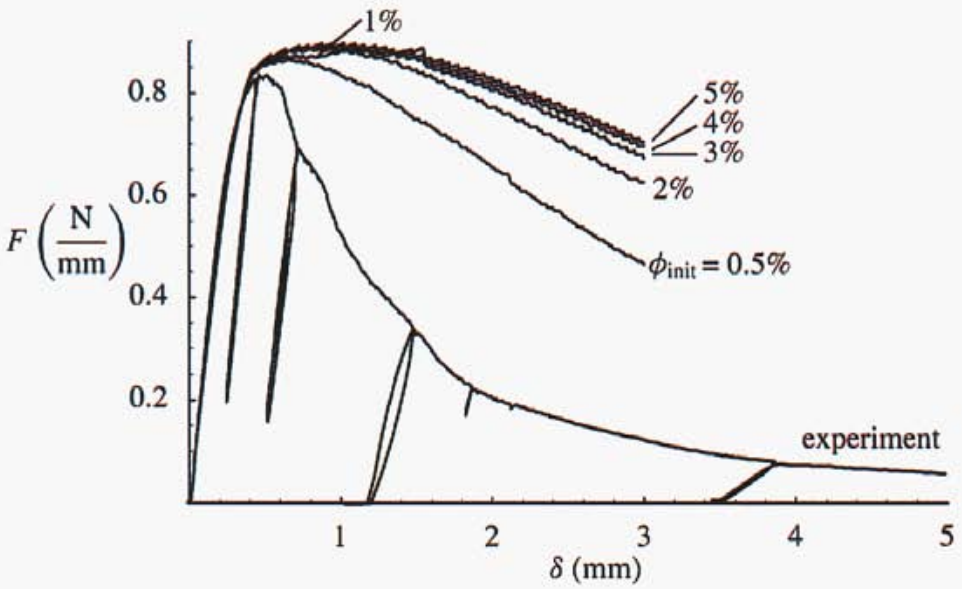

Figure 4.10: Comparison of the force versus line-load displacement measured in the experiments and computed for different values of ϕ_{init}. Load reversals are not performed in the simulations.

Figure 4.10 compares the force versus displacement at the center loading pin from the experiments with simulations results for $\phi_{\text{init}} = \{0.5, 1, 2, 3, 4, 5\}\%$. Load reversals performed in the experiments are not included in the boundary conditions for the simulations. The simulation results match the experimental measurements up to the point at which the load begins to plateau. The correspondence over this portion of the loading indicates the simulations are capable of reproducing gross structural response resulting from the beam dimension, the initial crack length, and the material properties of the bulk material. The peak in the response is due to the onset of plastic flow, while the subsequent drop in load is the result of crack extension. The simulations predict the peak load reasonably well, but the post-peak response differs significantly. As described in Section 4.1, the model parameters considered in this study overpredict the work to fracture for this material, and the results shown in this figure are consistent with that observation. The variation in the results with ϕ_{init} indicate we would need to choose $\phi_{\text{init}} < 0.5\%$ in order to achieve better agreement with the experimental observations.

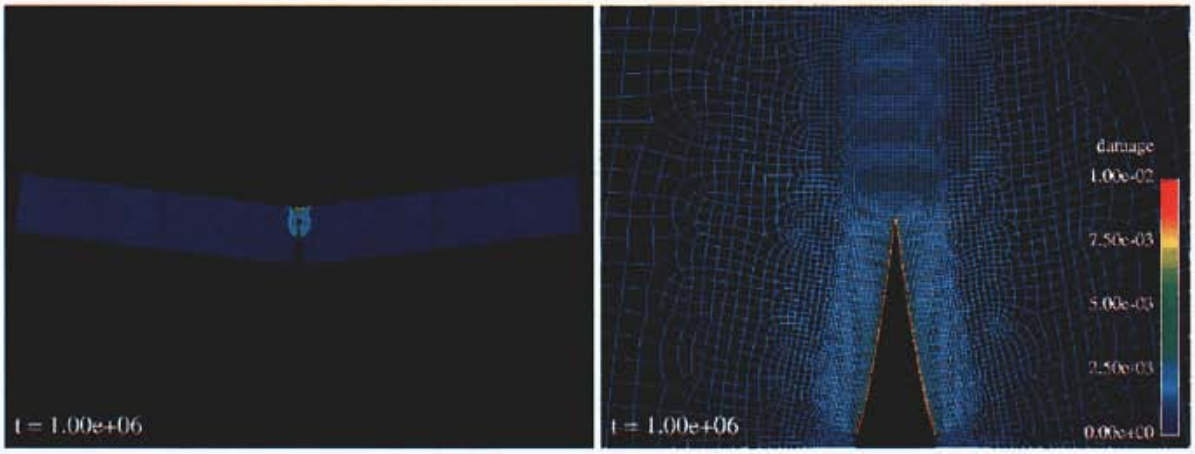

(a) (b)

Figure 4.11: Results of the three-point bending calculations with $\phi_{\text{init}} = 0.5\%$ showing (a) contours of the equivalent plastic strain plotted over the entire beam geometry and (b) a near tip view of the mesh colored by the damage ϕ.

Figure 4.11(a) shows the final configuration of the beam and contours of plastic strain for $\phi_{\text{init}} = 0.5\%$. The contours of plastic strain display the pattern characteristic of the three-point bending configuration. Figure 4.11(b) shows a near tip view of the damage over an outline view of the mesh. As expected, damage is strongly concentrated along the surfaces of the crack. The sequence of images in Figure 4.12 shows the evolution of the plastic strain with crack extension for $\phi_{\text{init}} = 0.5\%$. Plasticity begins by forming a thin band connecting the initial crack tip position with the area contacted by the center loading pin. This band is widened by the moving crack tip. The specimens in the experiments have side grooves on the surface to suppress the formation of shear lips, so this pattern of plasticity was not evident on the surface.

In summary, the simulations are able to predict certain aspects observed in the experiments; however, the fracture resistance predicted by the calculations exceeds what is observed in the experiments, as was the case with the simulations in Section 4.1. Better parameters need to be determined for the model before attempting to model the more complicated loading conditions applied in the experiment, which include load reversals and asymmetric beam configurations. The simulations do demonstrate that laboratory experiments of ductile fracture can be modeled at a level of fidelity that captures all the relevant length scales in the problem. The simulations also point out that detailed information about the deformation surrounding the crack tip is necessary are needed to improve the model predictions.

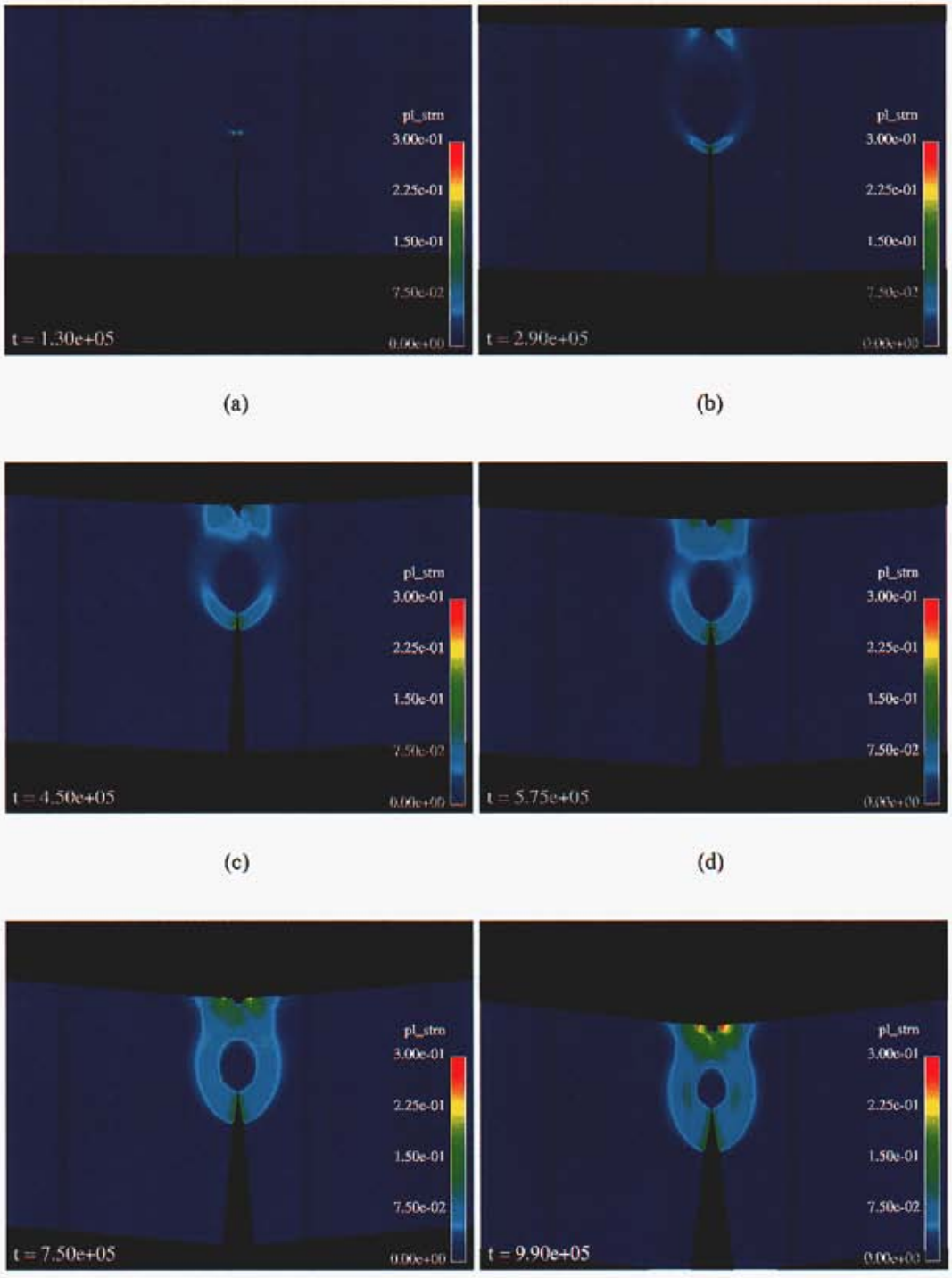

Figure 4.12: A sequence of images showing contours of the equivalent plastic strain for the case $\phi_{\text{init}} = 0.5\%$. The time t shown is expressed in 10^{-4} seconds.

Chapter 5

Summary

5.1 Conclusions

In this work, we develop thermodynamically consistent cohesive zone relations for modeling fracture in ductile materials. The cohesive relations are in the form of rate equations for the evolution of the opening displacements and internal state variables as a function of the current state and the applied traction. The models exhibit purely inelastic response, which contributes to their ability to ensure traction continuity in time when the cohesive relations are activated. Expressed as rate equations, the cohesive relations readily admit transitions between rigid response and flow, depending on the traction and current state of the material in the zone. We employ an augmented Lagrangian approach for enforcing the displacement constraints under conditions when the cohesive relations predict rigid response. We developed a nodal integration scheme for integrating the variational equations over the cohesive zone which is used both during states of constraint and flow to produce smooth switching between the states.

The SEM straining experiments effectively illustrated plastic zone development in fracture specimens containing cracks. The specimen size restrictions imposed by both the SEM environment and modeling considerations prevented the observation of fracture in 304L specimens. Recent experiments involving similarly sized three-point bend geometry specimens of forged 21-6-9 stainless steel have shown stable crack growth. Because 21-6-9 is an important alloy in gas transfer systems, inclusion of this alloy in future modeling efforts may be of interest. The EBSD pattern quality approach to mapping plastic zones using digital pattern capture and image analysis techniques failed to distinguish between calibration specimens subjected to different levels of plastic strain. The promise of this technique to provide high-resolution plastic zone mapping warrants further effort. However, that effort would best be carried out in an organization with direct access to facilities for electron microscopy.

The example calculations demonstrated regularization provided by the cohesive zone even in the situation where a geometric singularity still exists in the mesh, that is, there is a geometric crack tip for which the opening displacements are enforced to be zero through imposition of constraints. With cohesive models like the one proposed by Xu and Needleman [31], the initial compliance effectively removes geometric singularities as well as the possibility for singular stresses. With

the initially rigid cohesive relations, there is still a sharp crack tip and the role of the cohesive tail is to remove the stress singularity resulting from the geometric singularity. Using parameters for the evolution relations in the cohesive zone model from values determined for the associated bulk model and combining these with parameters like the localized zone width w_0 inferred from the micrographs, the simulations were able to reproduce features observed in the experiments with some accuracy. At a local scale, the simulations predicted a process zone length of 300μm which is within a factor of two what can be seen in the micrographs. Macroscopically, the peak stress predicted for the three-point bending tests agreed very well with the experimental results. However, the calculations overpredicted the work to fracture for the 6061-T6 material used in the experiments. Although the simulation results did not reproduce all aspects of the crack growth behavior observed in the experiments, the simulations do demonstrate that laboratory experiments of ductile fracture can be modeled at a level of fidelity that captures all the relevant length scales in the problem.

The progress achieved in this study suggests many avenues for future work:

(i) Stability of traction integration with $m > 1$. We experienced instabilities in the traction integration scheme for values of the damage evolution exponent $m > 1$. The instabilities became more severe as m increased. This parameter describes the stress concentrating effect of porosity in the zone and is a key parameter defining the traction evolution. Additional work is required to develop stabilized integration schemes that would allow greater flexibility in selecting m.

(ii) The role of defects in initiating localized deformation. The results of the simulations with varying ϕ_{init}, the level of damage at which the cohesive relations becomes active, indicate unusually low values ($\phi_{\text{init}} < 0.5\%$) would be needed to reproduce the experimental results. This conclusion suggests defects may be playing a key role in triggering the localized deformation at the crack tip. This assumption is supported by the *in situ* observations which clearly show the crack path meandering between sources of stress concentration, such as second phase particles, grain boundaries, or the intersections of persistent slip bands. The detailed role these defects play at the head of a growing crack are not well understood.

(iii) Rate and thermal effects. The calculations presented in this work intentionally considered loading conditions that would not trigger the inherent rate-dependencies in the cohesive model. The rate effects combined with the temperature dependence in the model needs to be investigated over a broader range of experimental conditions.

(iv) Load reversals. Load reversals reveal information about the detailed structure of the deformation and state of the material around the crack tip. Simulations including load reversals should be exploited to see the predictive capability of the modeling approach.

(v) Three-dimensional and mixed-mode effects. Shear lips and other variations in the plastic deformation through the thickness of the specimen provide severe tests of the predictive capabilities of the model under general conditions of loading. Mixed-mode loading conditions, which may be investigated in two-dimensions as well, also provide an opportunity to investigate the predictive capability of the modeling approach.

(vi) Improved experimental methods. Cohesive relations are process models. Macroscopic results do provide some means for validating the model predictions; however, only detailed information about the near tip region can reveal whether the mechanisms embedded in the cohesive relations evolve as intended. We were unable to develop a method to map the plastic strains within a small region surrounding the crack tip. This information is essential for understanding the interaction between the bulk material and the fracture process zone. For experiments conducted at higher rates, thermal imaging provides one option for determining the extent of plastic deformation. The role of defects in triggering localized deformation must be investigated experimentally before models for these triggering mechanisms can be incorporated in a cohesive modeling approach.

5.2 Acknowledgements

This work was performed at Sandia National Laboratories. Sandia is a multiprogram laboratory operated by Sandia Corporation, a Lockheed Martin Company, for the U.S. Department of Energy under contract DE-AC04-94AL85000.

This page intentionally left blank.

Bibliography

[1] D.J. Bammann, *Modeling temperature and strain rate dependent large deformations of metals*, Applied Mechanics Reviews **1** (1996), 312–318.

[2] D.J. Bammann, M.L. Chiesa, and G.C. Johnson, *Modeling large deformation and failure in manufacturing processes*, Theoretical and Applied Mechanics (1996), 359–376.

[3] A.C.F. Cocks and M.F. Ashby, *Intergranular fracture during power-law creep under multiaxial stress*, Metall. Sci. **14** (1980), 395–402.

[4] B.D. Coleman and M.E. Gurtin, *Thermodynamics with internal state variables*, The Journal of Chemical Physics **47** (1967), 597–613.

[5] A. De-Andrés, J.L. Pérez, and M. Ortiz, *Elastoplastic finite element analysis of three-dimensional fatigue crack growth in aluminum shafts subjected to axial loading*, International Journal of Solids and Structures **36** (1999), 2231–2258.

[6] M.L. Falk, A. Needleman, and J.R. Rice, *A critical evaluation of cohesive zone models of dynamic fracture*, Journal de Physique IV **11** (2001), 43–50.

[7] H.J. Frost and M.F. Ashby, *Deformation-mechanism maps*, Pergamon Press, New York, 1982.

[8] A.L. Gurson, *Continuum theory of ductile rupture by void nucleation and growth: PART I*, Journal of Engineering Materials and Technology **99** (1977), 2–15.

[9] M.R. Hestenes, *Multiplier and gradient methods*, Journal of Optimization Theory and Application **4** (1969), 303–320.

[10] R. Hill, *Acceleration waves in solids*, Journal of the Mechanics and Physics of Solids **10** (1962), 1–16.

[11] G.R. Irwin, *Analysis of stresses and strains near the end of a crack traversing a plate*, Journal of Applied Mechanics **24** (1957), 361–364.

[12] P.A. Klein, J.W. Foulk, E.P. Chen, S.A. Wimmer, and H.J. Gao, *Physics-based modeling of brittle fracture: cohesive formulations and the application of meshfree methods*, Theoretical and Applied Fracture Mechanics **37** (2001), 99–166.

[13] P.A. Klein, H. Gao, Vainchtein A., Fujimoto H., J. Lee, and Q. Ma, *Micromechanics-based modeling of interfacial debonding in multilayer structures*, Thin Films Stresses and Mechanical Properties VIII (R. Vinci, O. Kraft, N.R. Moody, and E. Besser, P.R.and Shaffer, eds.), vol. 594, Materials Research Society, 2000.

[14] D. Krajcinovic, *Continuum damage mechanics*, Applied Mechanics Reviews **37** (1984), 1–6.

[15] K.D. Papoulia, C.-H. Sam, and S. Vavasis, *Time continuity in cohesive finite element modeling*, International Journal for Numerical Methods in Engineering **58** (2002), 679–701.

[16] M.J.D. Powell, *A method for nonlinear constraints in minimization problems*, Optimization (R. Fletcher, ed.), Academic Press, London, 1965.

[17] L. Prandtl, *Ein Gedankenmodell für den Zerreißvorgang spröder Körper*, Zeitschrift für angewandte Mathematik und Mechanik **13** (1933), 129–133.

[18] T. Siegmund and W. Brocks, *Prediction of the work of separation and implications to modeling*, International Journal of Fracture **99** (1999), 97–116.

[19] T. Siegmund and A. Needleman, *A numerical study of dynamic crack growth in elastic-viscoplastic solids*, International Journal of Solids and Structures **34** (1997), 769–787.

[20] J.C. Simo and T.J.R. Hughes, *Computational inelasticity*, Springer, New York, 1998.

[21] G.I. Taylor and H. Quinney, *The latent energy remaining in a metal after cold working*, Proceedings of the Royal Society **A143** (1934), 307–326.

[22] P.F. Thomason, *Ductile fracture and the stability of incompressible plasticity in the presence of microvoids*, Acta Metallurgica **29** (1981), 763–777.

[23] A.T. Tucker, A.J. Wilkinson, M.B. Henderson, H.S. Ubhi, and J.W. Martin, *Measurement of fatigue crack plastic zones in fine grained materials using electron backscattered diffraction*, Materials Science and Technology **16** (2000), 427–430.

[24] V. Tvergaard and J.W. Hutchinson, *The relation between crack growth resistance and fracture process parameters in elastic-plastic solids*, Journal of the Mechanics and Physics of Solids **40** (1992), 1377–1397.

[25] ———, *Toughness of an interface along a thin ductile layer joining elastic solids*, Philosophical Magazine A **70** (1994), 641–656.

[26] A. Uguz and J.W. Martin, *Plastic zone size measurement techniques for metallic materials*, Materials Characterization **37** (1996), 105–118.

[27] A.G. Varias, *Constraint effects during stable transient crack growth*, Computational Mechanics **21** (1998), 316–329.

[28] A.J. Wilkinson and D.J. Dingley, *Quantitative electron diffraction studies using electron back scatter patterns*, Acta Metall Materialia **39** (1991), 3047–3055.

[29] _____, *The distribution of plastic deformation in a metal matrix composite caused by staining transverse to the fiber direction*, Acta Metall Materialia **40** (1992), 3357–3368.

[30] A.J. Wilkinson and P.B. Hirsch, *Electron diffraction based techniques in scanning electron microscopy of bulk materials*, Micron **28** (1997), 279–308.

[31] X.-P. Xu and A. Needleman, *Numerical simulations of fast crack growth in brittle solids*, Journal of the Mechanics and Physics of Solids **42** (1994), 1397–1434.

DISTRIBUTION

1	MS 0427	J.R. Weatherby, 2134
1	MS 0835	K.F. Alvin, 9142
1	MS 0847	J. Jung, 9127
1		G.W. Wellman, 9127
1	MS 0847	S.W. Attaway, 9134
1	MS 0847	M.L. Blanforth, 9142
1		A.S. Gullerud, 9142
1		S.W. Key, 9142
1		J.R. Koteras, 9142
1		J.A. Mitchell, 9142
1	MS 0893	J. Pott, 9123
1		R.S. Chambers, 9123
1		J.V. Cox, 9123
1		C.S. Lo, 9123
1		E.D. Reedy, 9123
1		W.M. Scherzinger, 9123
1	MS 9014	D.M. Kwon, 8242
1		A.R. Ortega, 8242
1	MS 9042	G.J. Wagner, 8752
5	MS 9042	B.R. Antoun, 8754
1		D.B. Dawson, 8754
1	MS 9042	P.A. Spence, 8774
1		M.L. Chiesa, 8774
1		J.J. Dike, 8774
1		P.M. Gullett, 8774
1		M.D. Jew, 8774
1		B.L. Kistler, 8774
1		Y. Ohashi, 8774
1		J.T. Ostien, 8774
1		V.D. Revelli, 8774

1	MS 9161	W.R. Even, 8760
1	MS 9161	E.P. Chen, 8763
1		C.J. Kimmer, 8763
10		P.A. Klein, 8763
1		J.A. Zimmerman, 8763
1	MS 9402	D.F. Cowgill, 8772
1		B.P. Somerday, 8772
1	MS 9403	N.Y.C. Yang, 8773
1	MS 9405	J.M. Hruby, 8700
1	MS 9405	S. Aubrey, 8763
5		D.J. Bammann, 8763
1		A.A. Brown, 8763
1		G.R. Feijoo, 8763
5		J.W. Foulk, 8763
1		R.E. Jones, 8763
1		E.B. Marin, 8763
1		R.A. Regueiro, 8763
1	MS 9409	J.R. Garcia, 8754
1		S.H. Goods, 8754
5		S.X. McFadden, 8754
1		N.R. Moody, 8754
3	MS 9018	Central Technical Files, 8945-1
1	MS 0899	Technical Library, 9616
1	MS 9021	Classification Office, 8511 for Technical Library, MS 0899, 9616 DOE/OSTI via URL
1	MS 0323	D.L. Chavez, LDRD Office, 1011

This page intentionally left blank.